Journal of Molecular Structure 1231 (2021) 129950

Contents lists available at ScienceDirect

Journal of Molecular Structure

journal homepage: www.elsevier.com/locate/molstr

Novel structurally characterized Co(II) metal-organic framework and Cd(II) coordination polymer self-assembled from a pyridine-terminal salamo-like ligand bearing various coordination modes

Ji-Fa Wang[a], Tao Feng[a], Ya-Juan Li[a], Yin-Xia Sun[a], Wen-Kui Dong[a,*], Yu-Jie Ding[b,*]

[a] School of Chemical and Biological Engineering, Lanzhou Jiaotong University, Lanzhou, Gansu, 730070, China
[b] College of Biochemical Engineering, Anhui Polytechnic University, Wuhu 241000, China

ARTICLE INFO

Article history:
Received 14 August 2020
Revised 23 October 2020
Accepted 13 January 2021
Available online 19 January 2021

Keywords:
Salamo-like ligand
Coordination polymer
Metal-organic framework
TGA analysis
Hirshfeld surface analysis

ABSTRACT

Two novel structurally characterized Co(II) metal-organic framework (Co(II) MOF) and Cd(II) coordination polymer (Cd(II) CP), $[\{Co(L)\}_2]_n \cdot nCH_3COCH_3$ and $[Cd(H_2L)(CH_3COO)_2]_n$ were self-assembled from a newly designed salamo-like ligand H_2L bearing double terminal pyridine groups and Co(II) and Cd(II) ions, respectively. In the Co(II) MOF, the Co1 and Co2 ions are six-coordinated octahedron geometries, have similar coordination environments, and are located in the N_2O_2 cavities of the ligand $(L)^{2-}$ units, forming "Co1-L" and "Co2-L" parts, respectively. The terminal pyridine N atoms of the "Co1-L" (or "Co2-L") part are connected with "Co1-L" and "Co2-L" parts respectively, forming a metal-organic framework with double helix structure in the*a*-direction and regular channels in the *c*-direction. In the Cd(II) CP, Cd(II) ion is seven-coordinated single cap triangular prism geometry, did not participate in the coordination of the N_2O_2 cavity, but coordinated with free acetate in the solution. Two bidentate acetate anions chelate to Cd1 ion, and two Cd1 ions are bridged by O atom of one of the acetate anions to form $Cd_2(OAc)_2$ unit which was used as the junction point to connect with the terminal pyridine N atoms of H_2L. Finally, the coordination polymer with large pore channels was formed. Spectroscopic analyses of H_2L and its Co(II) MOF and Cd(II) CP are performed using IR, UV–Vis and fluorescence spectroscopy. TGA analyses show that the Co(II) MOF and Cd(II) CP have good stabilities. Various short-range interactions in the Co(II) MOF and Cd(II) CP are investigated through Hirshfeld surfaces analyses.

1. Introduction

Metal-organic frameworks (MOFs) [1–7] and coordination polymers (CPs) [8–14] are attracting more and more attention due to their regular pore channels with large porosity. In 2017, Guo et al. constructed a MOF using a pyridyl-terminal base ligand with auxiliary ligand and applied to selectively separate Th(IV) from Ln(III) [15]. In 2017, Dong et al. reported 2 salen-like ligands containing pyridine terminal group, that coordinated with Zn(II) by varying the ratio of the two ligands, resulted 3 six-membered cyclic CPs, enabling the chiral separation of different amino acids [16]. In 2018, on the basis of previous research, Ren et al. realized the replacement of metal ions in MOFs by introducing different metal ions, and obtained 6 isomorphic MOFs with excellent catalytic performance [17]. In 2019, Xia et al. developed a ligand containing pyridine groups, and constructed 3 isomorphic MOFs with terephthalic acid and Cd(II), which were studied for gas adsorption and could be used as excellent catalyst [18]. In 2020, Wang et al. synthesized 2 Co(II) coordination polymers and applied them to the degradation of dye molecules [19]. In 2020, Liu et al. synthesized 3 photochromic coordination polymers that offer the possibility of designing color-changing materials [20].

Salen- [21–27] and salamo-like compounds [28–34] are the more common and versatile ligands in modern coordination chemistry because they can provide stable N_2O_2 coordination sites, various metal salen- and salamo-like complexes with novel structures have been obtained. Because introduction of O atoms into alkyl chain, salamo-like compounds have better stability compared to salen-like ligands. Nearly decade, research of the salamo-like ligands and their metal complexes [34,35] has gradually deepened, and has been found that they have good application prospects in ion recognition [36–44], antibacterial activity [45–47], catalysis [48], luminescence [49,50], magnetism [51] and other fields, the theoretical researches are also carried out by DFT calculations [52] and Hirshfeld surfaces analyses [53–55].

* Corresponding authors.
E-mail addresses: dongwk@126.com (W.-K. Dong), yujieding123@163.com (Y.-J. Ding).

https://doi.org/10.1016/j.molstruc.2021.129950
0022-2860/

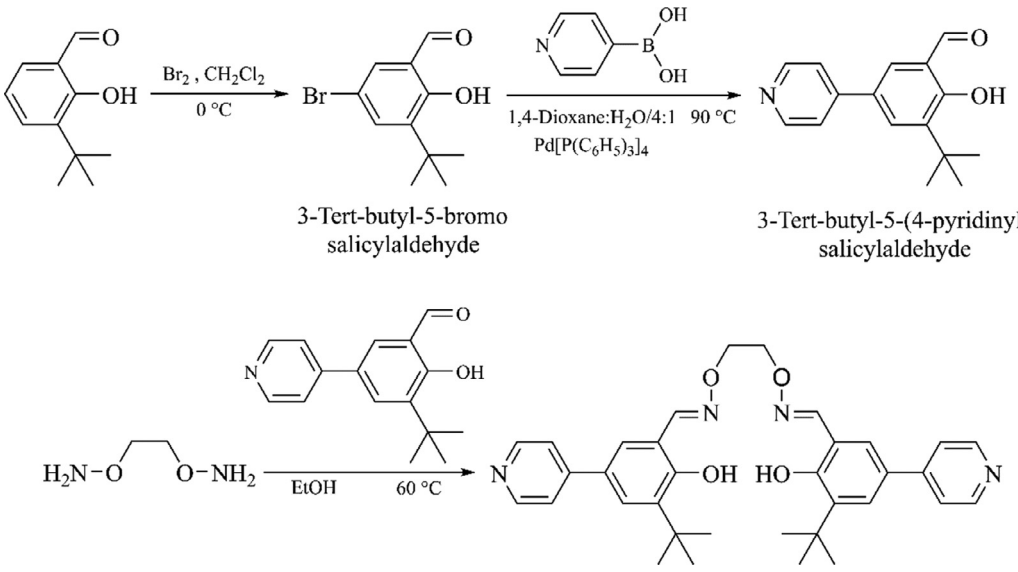

Scheme 1. Synthetic route to H_2L.

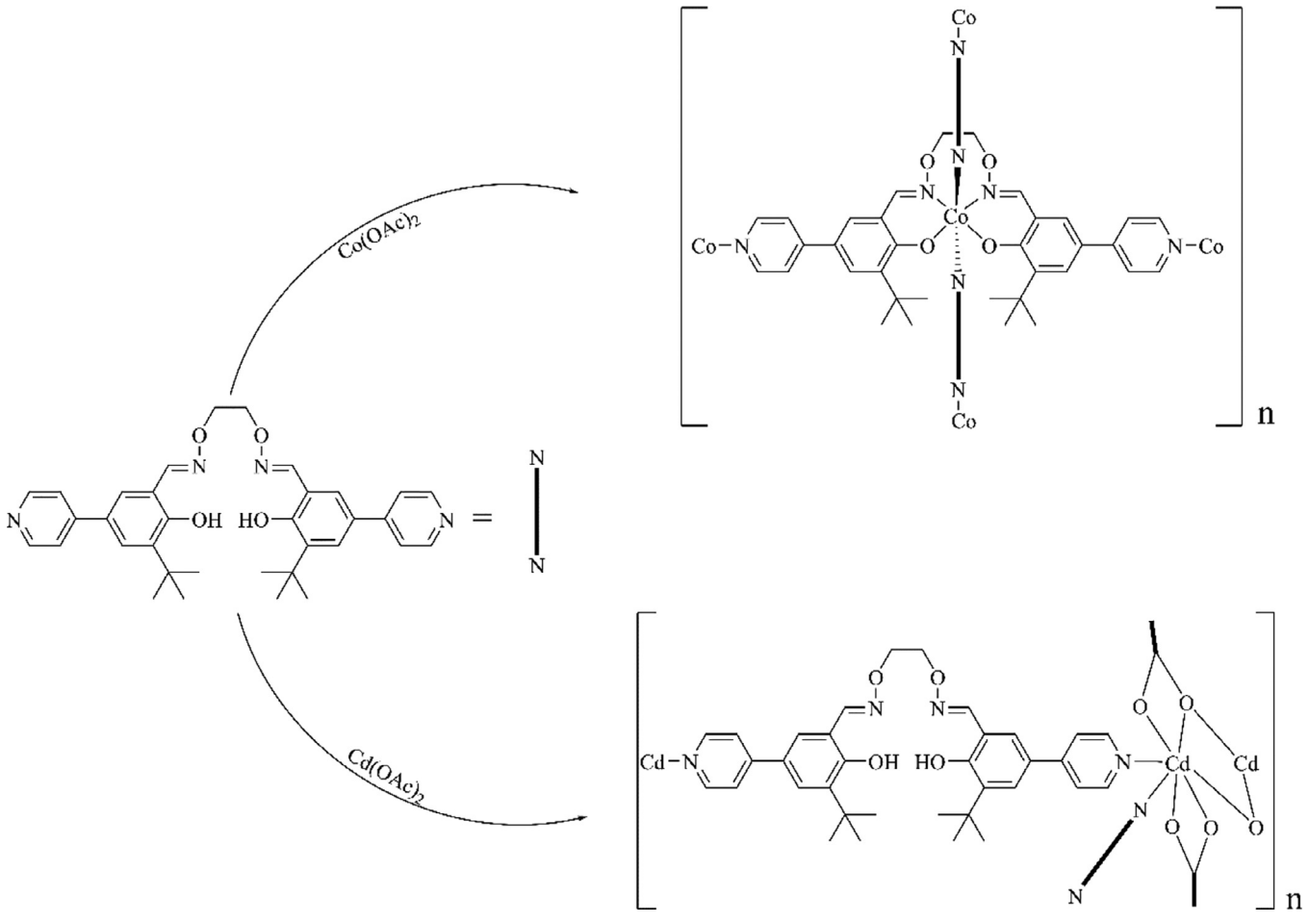

Scheme 2. Synthetic route to the Co(II) MOF and Cd(II) CP.

In conclusion, the introduction of terminal pyridine into the salen-like ligands [15–20] can provide two potential coordination sites. When different metal ions are added to the salen-like ligands, metal ions can participate in the coordination at different coordination sites, and various novel complexes such as MOFs can be self-assembled. Based on the in-depth study of salamo-like ligands, a novel salamo-like ligand H_2L braring double terminal pyridine groups was designed and synthesized. The Co(II) MOF and Cd(II) CP possessing novel structures are obtained by self-assembling of the ligand H_2L with Co(II) and Cd(II) ions, respectively. The coordination of the Co(II) and Cd(II) ions at different positions of the ligand H_2L gives rise to pore size differences.

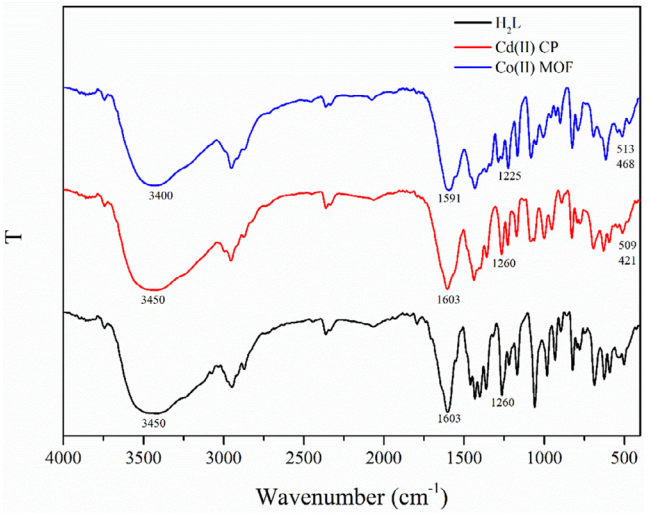

Fig. 1. IR spectra of H_2L and its Co(II) MOF and Cd(II) CP.

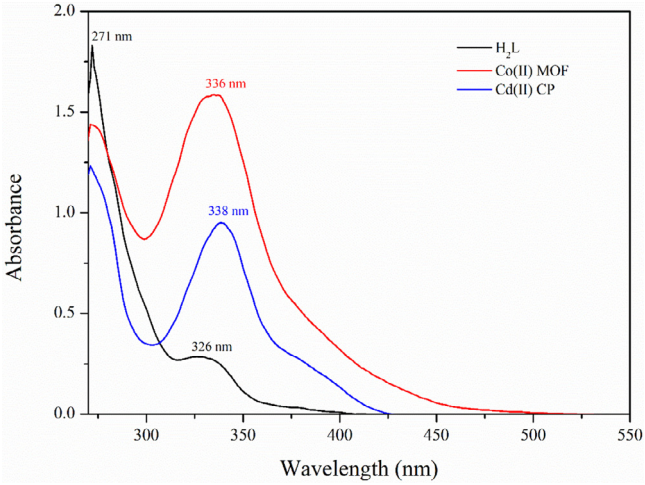

Fig. 2. UV–Vis spectra of H_2L and its Co(II) MOF and Cd(II) CP.

2. Experimental

2.1. Materials and general methods

All chemicals were analytical grade reagents from Shanghai Meiruier Chemical Technology Co., Ltd, solvents were analytical grade reagents from Tianjin Chemical Reagent Factory, and were used without further purification. Melting points were measured by the use of a microscopic melting point apparatus made by the Beijing Taike Instrument Limited Company and the thermometer was uncorrected. X-ray single crystal structure determinations were carried out on a SuperNova, Dual (Cu at zero) AtlasS2 CCD diffractometer. Other instruments used in the experiments can be found in our previously reported literature [45].

2.2. X-ray crystallographic analyses

X-ray single-crystal diffraction data of the Co(II) MOF was collected on a graphite monochromated Mo-K_α radiation (λ = 0.71073 Å) at 100 K for N_2 atmosphere. X-ray single-crystal diffraction data of the Cd(II) CP was collected on a graphite monochromated Cu-K_α radiation (λ = 1.54184 Å) at 100 K for N_2 atmosphere. The structures were solved by using the program (SHELXS-2015) [56,57], and Fourier difference techniques, and refined by full-matrix least-squares method on F^2. In the X-ray structure refinement, however, the solvent molecules of the Co(II) MOF and Cd(II) CP could not be located because of its high thermal disorder, and the final structure model was refined without the solvent molecules by using a SQUEEZE routine of PLATON, and the H atoms were included at the calculated positions and constrained to ride on their parent atoms. CCDC – 2014475 (The Co(II) MOF) and 2014474 (The Cd(II) CP) contain the supplementary crystallographic data for this paper.

2.3. Synthesis of the ligand H_2L

2.3.1. Synthesis of 3–tert–butyl–5-bromosalicylaldehyde

The synthetic route to the ligand H_2L is shown in Scheme 1. According to the reference [15], 3–tert–butyl–salicylaldehyde (178.23 mg, 1.0 mmol) was dissolved in two-neck round bottom flask containing 20 mL of dichloromethane, 1.5 mL of liquid bromine was drawn with a syringe and injected into a constant pressure drop funnel containing 15 mL of dichloromethane. Keep the system sealed to a temperature of 0 °C. Slowly added the brominated dichloromethane solution to the round bottom flask, keep the temperature constant and react 1.5 h. After, anhydrous

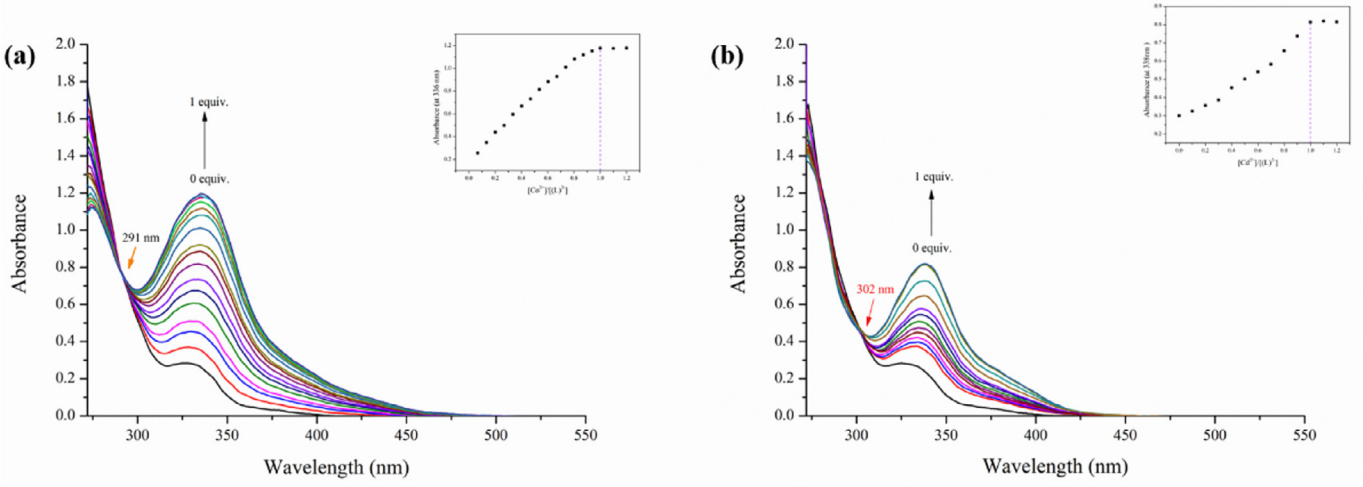

Fig. 3. (a) Continuous addition of Co^{2+} (1×10^{-3} M) to H_2L (5×10^{-5} M) leads to a change in absorbance intensity; (b) Continuous addition of Cd^{2+} (1×10^{-3} M) to H_2L (5×10^{-5} M) leads to a change in absorbance intensity.

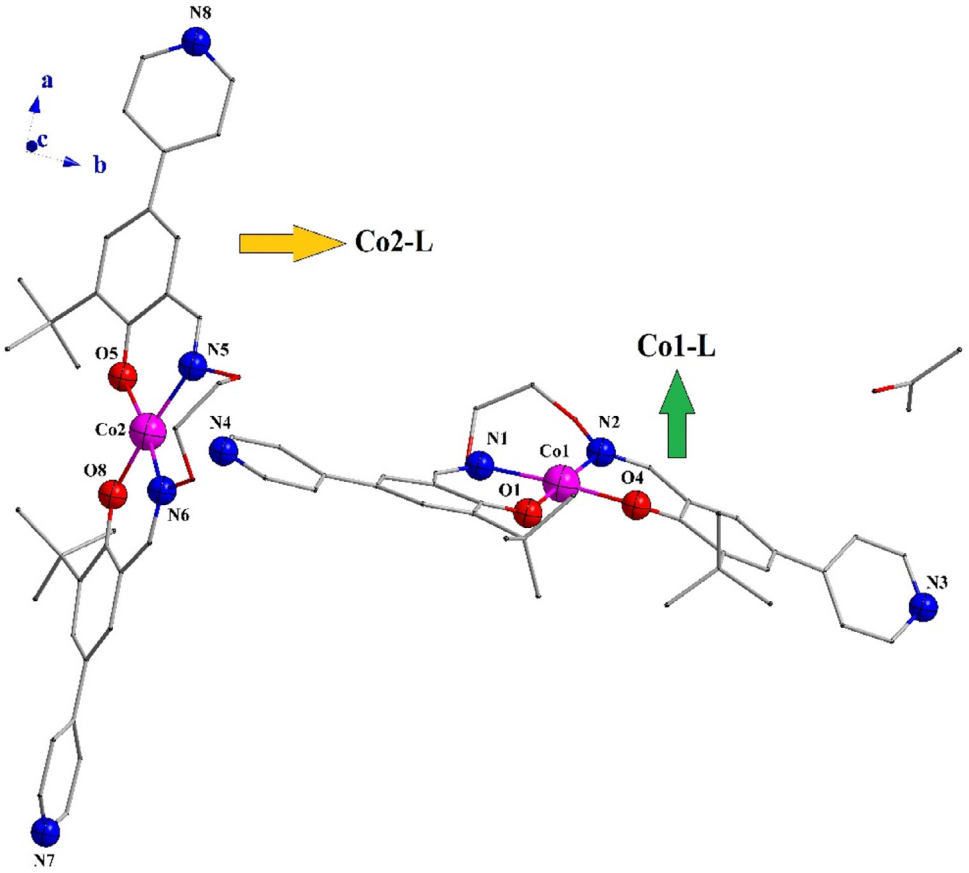

Fig. 4. Structure diagram of the "Co1-L" and "Co2-L" units.

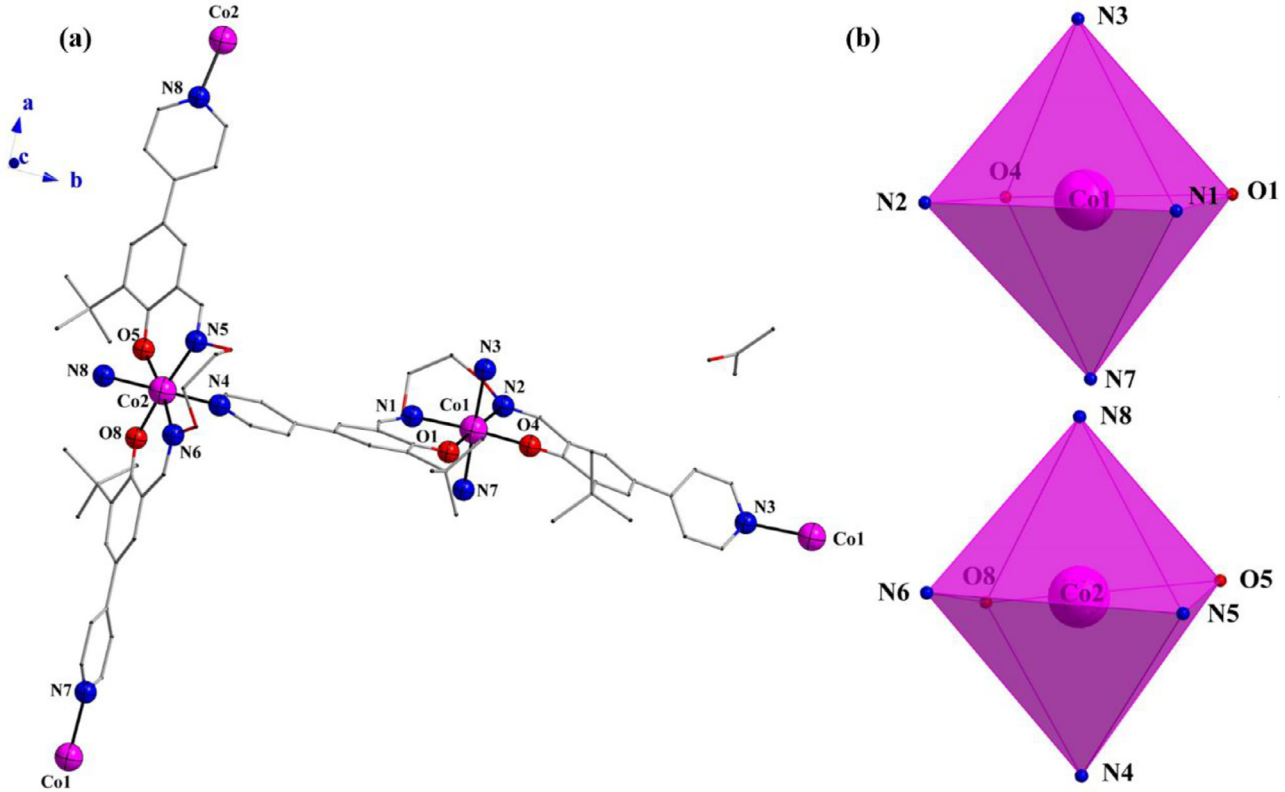

Fig. 5. (a) The smallest symmetric unit of the Co(II) MOF; (b) Coordination mode of the Co1 and Co2 ions.

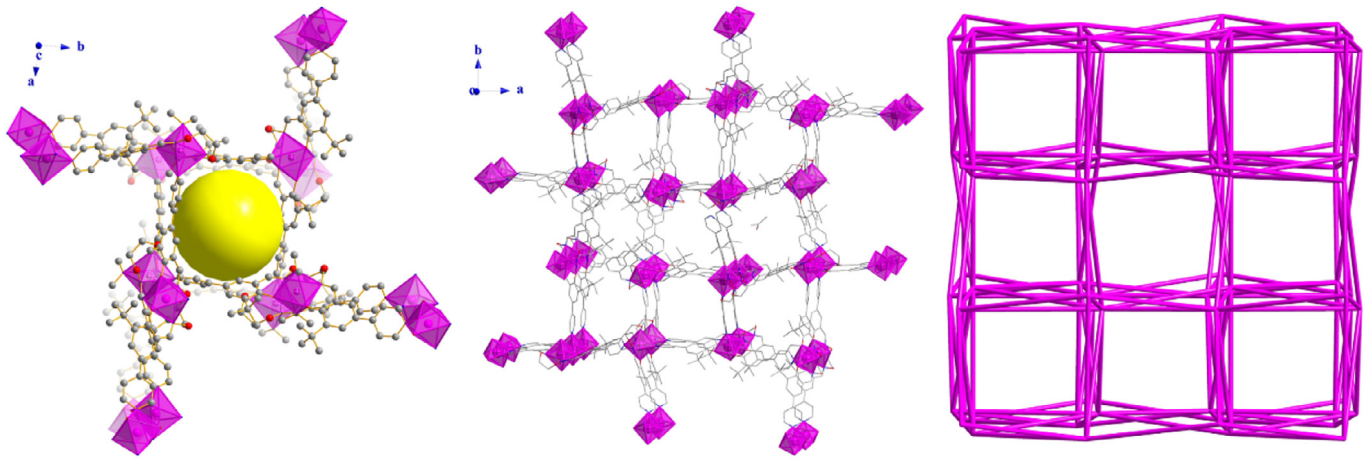

Fig. 6. Three-dimensional structure diagram of the Co(II) MOF in the*c*-direction.

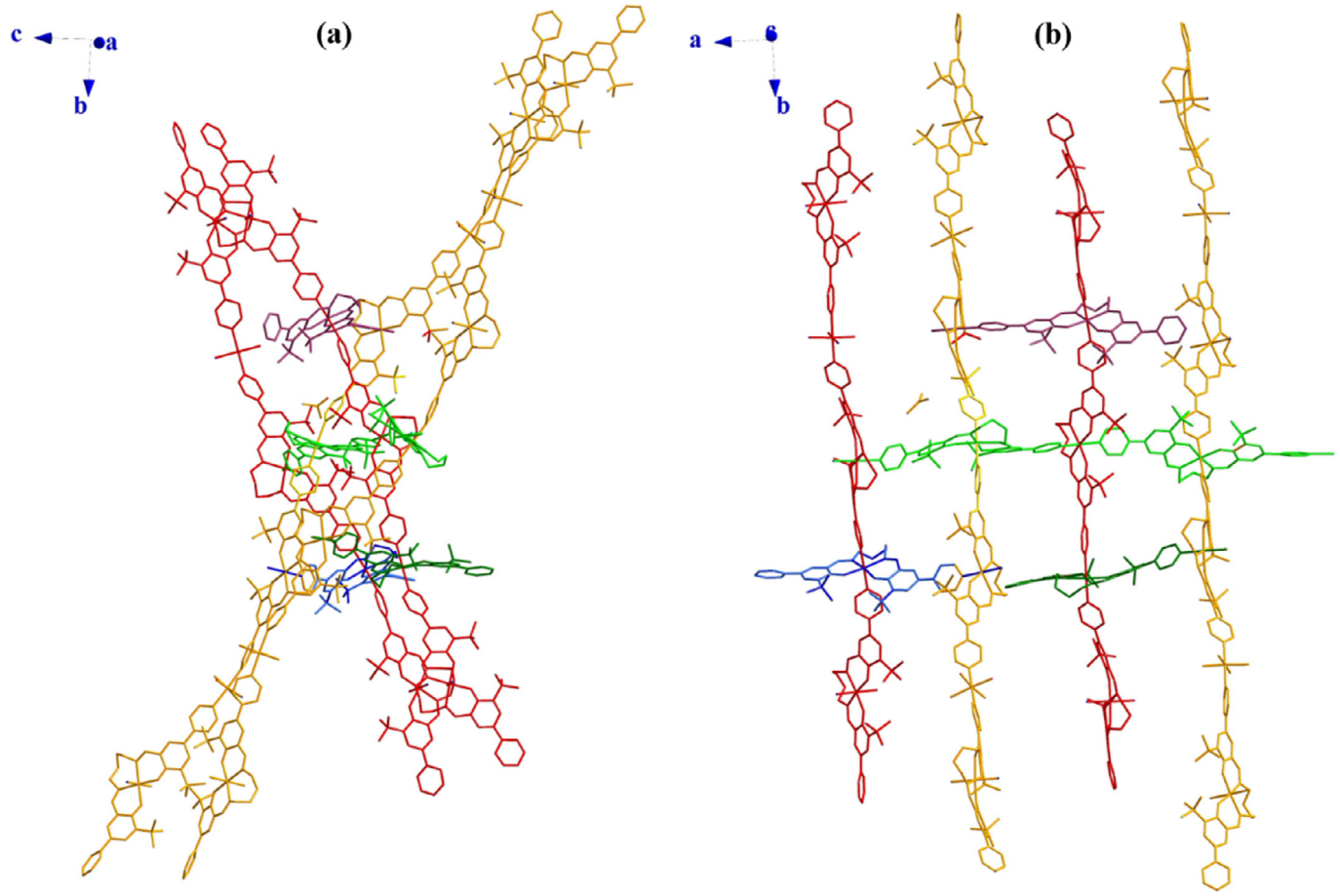

Fig. 7. (a) The double helix structure of the Co(II) MOF observed in the*a*-direction (red and yellow represent different helix structures respectively); (b) the intercalated double helix structure of the Co(II) MOF observed in the*c*-direction.

sodium sulfite solution (20 mL) was poured into the reactor and continued 0.5 h. Stop the reaction, the liquid was separated with a separating funnel, leaving the organic phase. It is then distilled under reduced pressure to give a bright yellow solid, namely 3–tert–butyl–5-bromosalicylaldehyde. ^{1}H NMR spectrum is shown in Fig. S1 (Supplementary Information). Yield: 91.8% (236.05 mg). M. p.: 62−64 °C. Anal. calcd. for $C_{11}H_{13}O_2Br$: C, 51.38; H, 5.10. Found: C, 51.81; H, 5.01. ^{1}H NMR (500 MHz, DMSO) δ 11.75 (s, 1H, -CHO), 9.96 (s, 1H, -OH), 7.89 (d, J = 2.5 Hz, 1H, -ArH), 7.57 (d, J = 2.5 Hz, 1H, -ArH), 1.37 (s, 9H, -CH_3).

2.3.2. Synthesis of 3–tert–butyl–5-(4-pyridinyl) salicylaldehyde

According to the reference [15], 3–tert–butyl–5-bromo-salicylaldehyde (1.28 g, 5 mmol), 4-pyridylboric acid (0.75 g, 6 mmol), $Pd(PPh_3)_4$ (0.23 g) and K_2CO_3 (2.08 g, 15 mmol) were added to a double port flask containing 50 mL of deaeration mixed solution (dioxane:distilled water = 4:1, V: V). Keep the system sealed and replace with N_2 to remove oxygen. Put the reaction system at 90 °C and reflux for 12 h, 40 mL dichloromethane and 50 mL distilled water were added after the solution was cooled to room temperature, separate with a separating funnel, leaved the

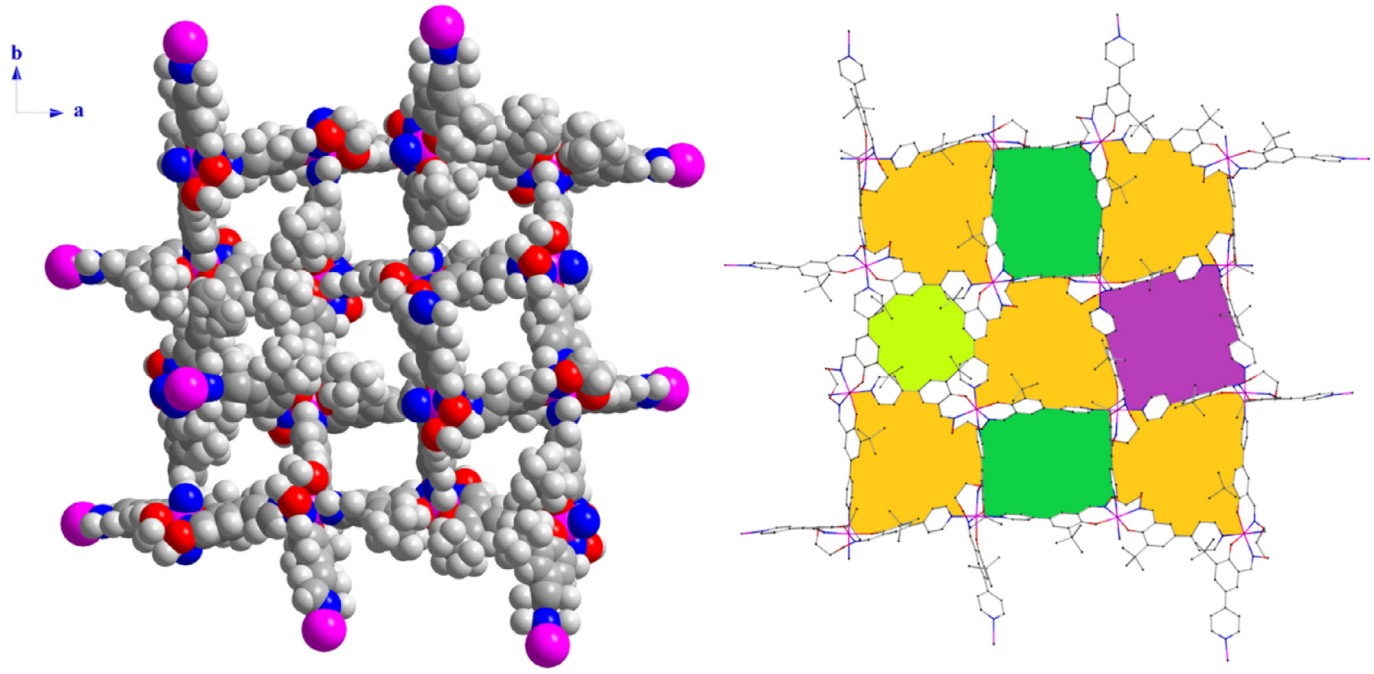

Fig. 8. Different pore sizes of the Co(II) MOF structure.

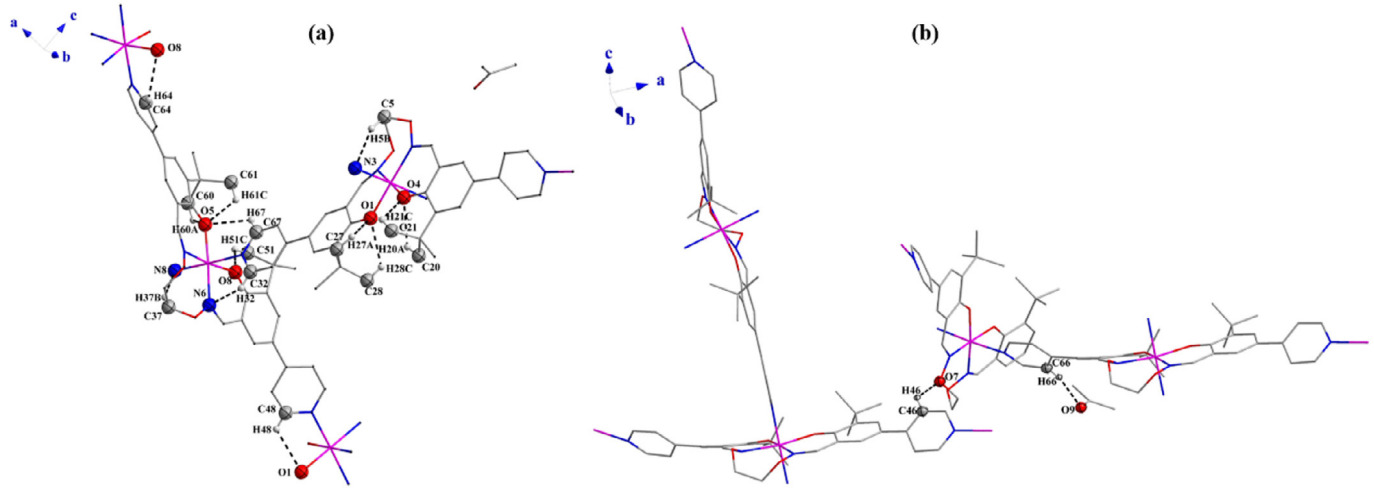

Fig. 9. (a) The intramolecular hydrogen bonds of the Co(II) MOF; (b) The intermolecular hydrogen bonds of the Co(II) MOF.

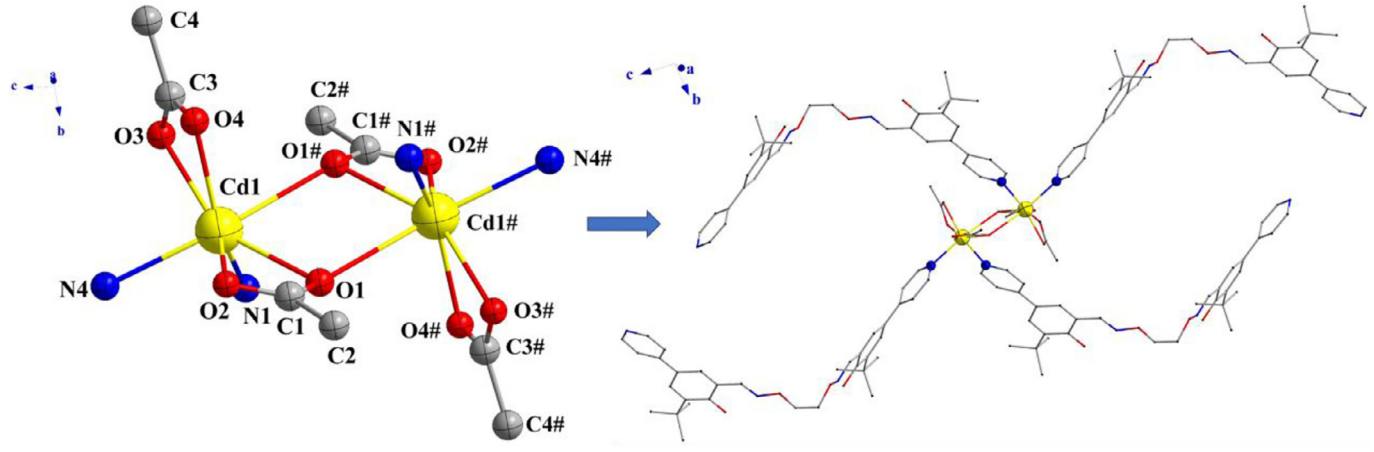

Fig. 10. The schematic diagram of the Cd(II) CP is constructed by taking $Cd_2(OAc)_2$ as the node.

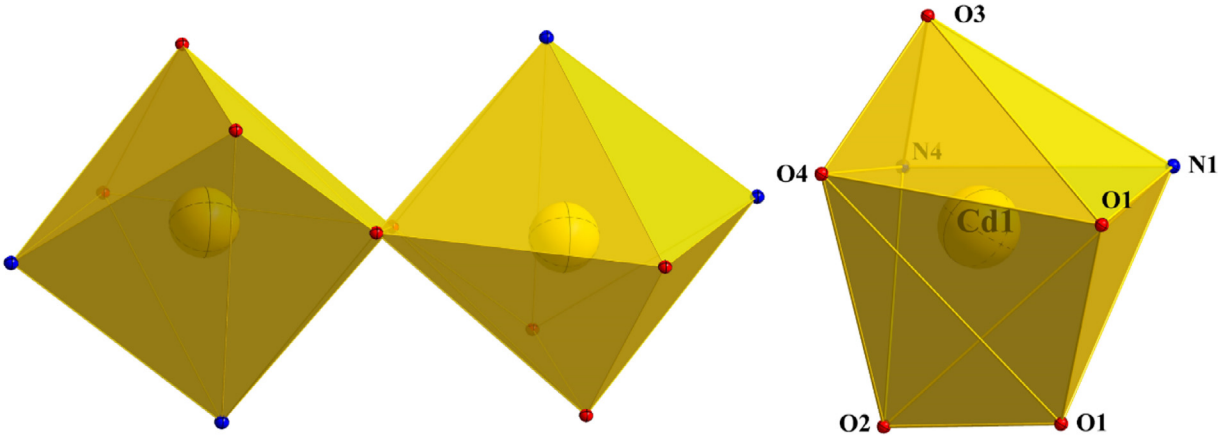

Fig. 11. Coordination modes of the Cd(II) ions.

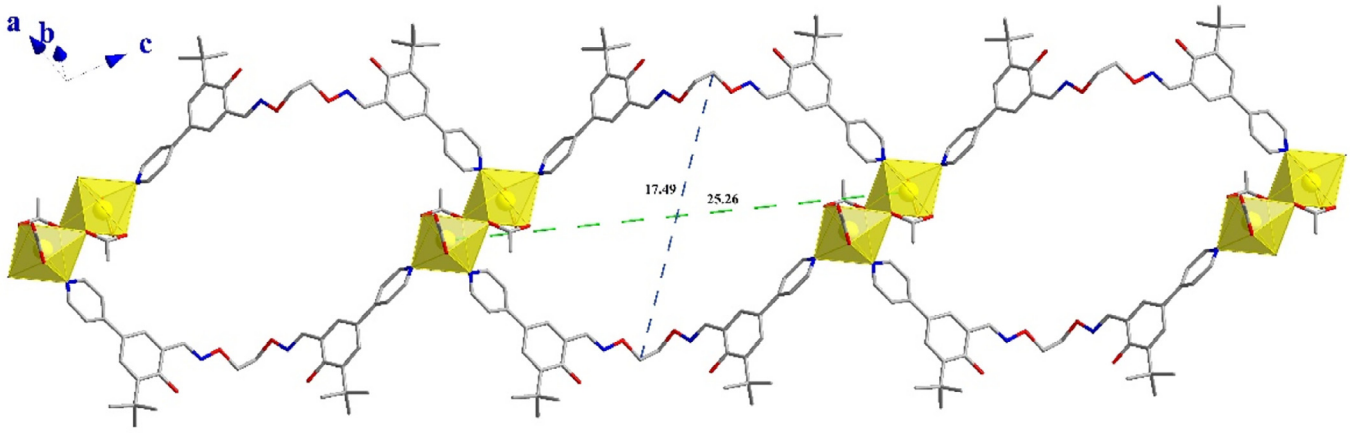

Fig. 12. The pore size of the Cd(II) CP.

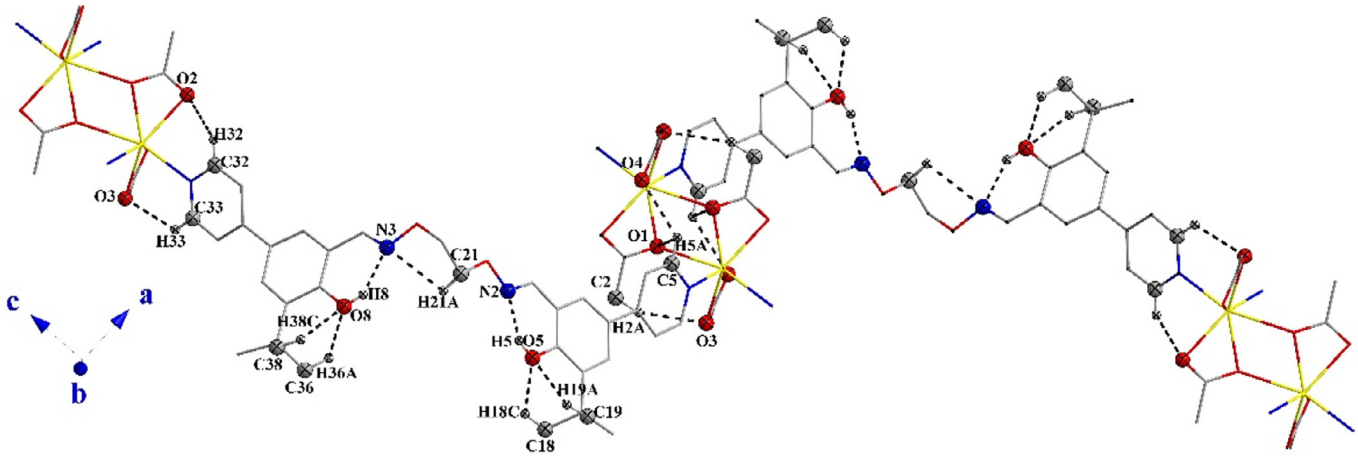

Fig. 13. The intramolecular hydrogen bonds of the Cd(II) CP.

organic layer, repeat the above operation for 3~4 times, and added anhydrous Na_2SO_4 to the organic layer. On the second day, after filtration and solvent removed, brown solid was obtained. After separation by column chromatography (ethyl acetate:petroleum ether = 1:1, V: V), yellow solid was obtained, namely 3–tert–butyl–5-(4-pyridyl) salicylaldehyde. ^{1}H NMR spectrum is shown in Fig. S2 (Supplementary Information). Yield: 50.2% (0.64 g). M. p.: 84–85 °C. Anal. calcd. for $C_{16}H_{17}NO_2$: C, 75.27; H, 6.71; N, 5.49. Found: C, 75.65.; H, 6.43; N, 5.12. ^{1}H NMR (500 MHz, CDCl3) δ 11.93 (s, 1H, -CHO), 9.98 (s, 1H, -OH), 8.66 (s, 2H, -ArH), 7.81 (s, 1H, -ArH), 7.69 (dd, J = 5.3, 1.6 Hz, 1H, -ArH), 7.49 (s, 2H, -ArH), 1.48 (s, 9H, -CH_3).

2.3.3. Synthesis of the ligand H_2L

1,2-Bis(aminooxy)ethane was synthesized according to the reported reference [48]. 10 mL of anhydrous ethanol of 1,2-bis(aminooxy)ethane (0.21 g, 2.28 mmol) was added to 1.14 g (4.47 mmol) of 3–tert–butyl–5-(4-pyridyl) salicylaldehyde of 20 mL anhydrous ethanol solution. Reaction at 60 °C for 12 h. When the temperature is reduced to 20 °C, a white solid was precipitate. ^{1}H

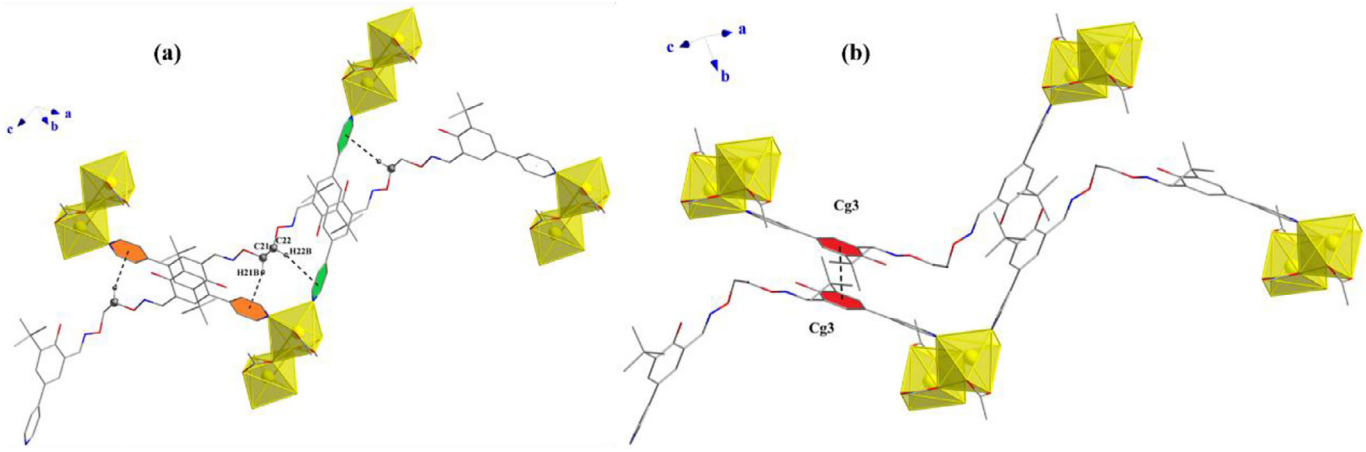

Fig. 14. (a) C–H···π interactions of the Cd (II) CP; (b) π···π stacking interactions of the Cd(II) CP.

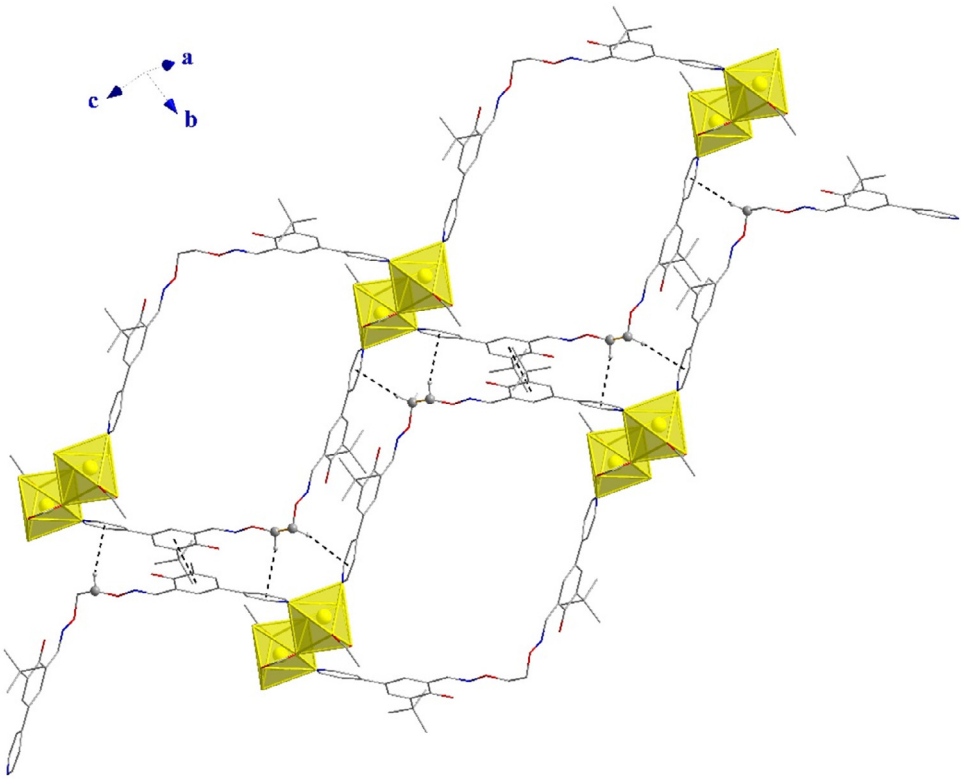

Fig. 15. 2-D supramolecular structure of the Cd(II) CP.

NMR spectrum of H_2L is shown in Fig. S3 (Supplementary Information). Yield: 57.6% (744.24 mg). M. p.: 129−131 °C. Anal. calcd. for $C_{34}H_{38}N_4O_4$: C, 72.06; H, 6.76; N, 9.89. Found: C, 72.34; H, 6.71; N, 9.82. ^{1}H NMR (500 MHz, $CDCl_3$) δ 10.55 (s, 1H, -OH), 8.62 (d, J = 6.0 Hz, 2H, -ArH), 8.34 (s, 1H, -*N*=CH), 7.57 (s, 1H, -ArH), 7.43 (d, J = 6.2 Hz, 2H, -ArH), 7.29 (s, 1H, -ArH), 4.56 (s, 2H, -CH_2), 1.47 (s, 9H, -CH_3). IR (cm^{-1}, KBr): 3450 (s), 1603 (s), 1260 (s).

2.4. Synthesis of the Co(II) MOF and Cd(II) CP

Synthetic route to the Co(II) MOF and Cd(II) CP are shown in Scheme 2.

The Co(II) MOF: 5.71 mg (0.01 mmol) H_2L was dissolved in 4 mL acetone, 2.52 mg (0.010 mmol) $Co(CH_3COO)_2{\cdot}4H_2O$ was dissolved in 2 mL anhydrous ethanol. The dissolved anhydrous ethanol solution was added into the acetone solution, the solution immediately turns orange red and became turbid during the stirring process. After 2 drops of pyridine was added into the solution, and the solution became clear. Continuously stirred for 20 min, then filtered, and sealed. After about 1 week, the red block-shaped single crystals suitable for X-ray diffraction were obtained. Yield: 53%. Although the single-crystal diffraction showed the product has the formula $[\{Co(L)\}_2]_n{\cdot}nCH_3COCH_3$, the product can be best formulated as $[\{Co(L)\}_2]_n{\cdot}3nCH_3COCH_3{\cdot}nC_5H_5N$ on the basis of microanalysis and TGA. Calcd for $C_{82}H_{95}Co_2N_9O_{11}$ (%): C, 65.63; H, 6.38; N, 8.40; Co, 7.85. Found (%): C, 65.92; H, 6.03; N, 8.11; Co, 7.74. IR (cm^{-1}, KBr): 3400 (s), 1591 (s), 1225 (s), 513 (m), 418 (m).

The Cd (II) CP: 5.72 mg (0.01 mmol) H_2L was dissolved in 3 mL acetone, 2.67 mg (0.010 mmol) $Cd(CH_3COO)_2{\cdot}H_2O$ was dissolved in 3 mL anhydrous ethanol. The dissolved anhydrous ethanol solution mentioned above was added dropwise into the acetone solution, the solution immediately turns

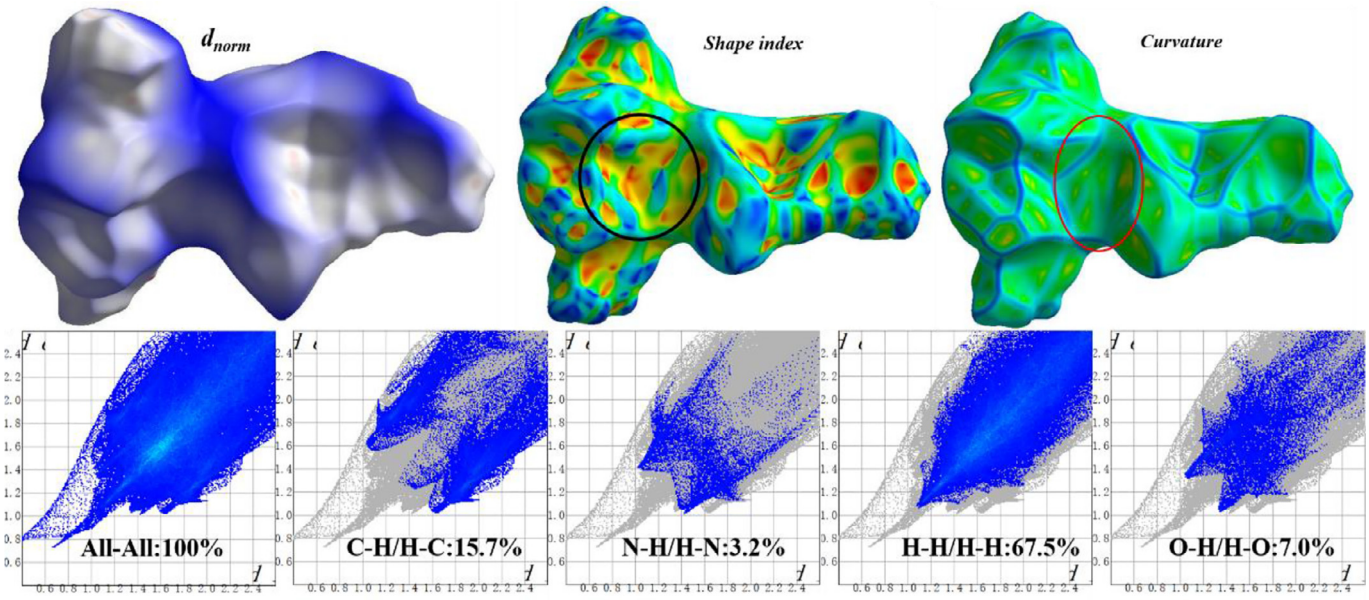

Fig. 16. Hirshfeld surface analysis mapping and various 2D fingerprints of the Co(II) MOF.

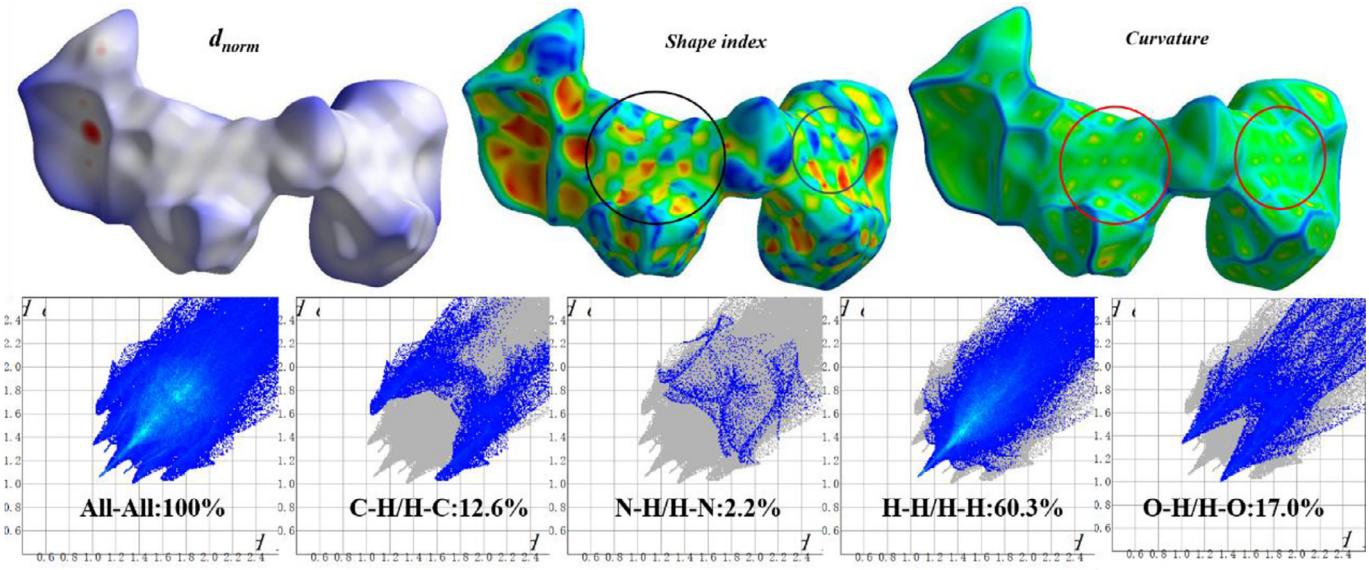

Fig. 17. Hirshfeld surface analysis mapping and various 2D fingerprints of the Cd(II) CP.

pale yellow, continue to stirred for 15 min, then filtered, sealed and remained still. After about 2 weeks, colorless block-shaped single crystals suitable for X-ray diffraction were obtained. Yield: 56%.

Although the single-crystal diffraction showed the product has the formula $[Cd(H_2L)(CH_3COO)_2]_n$, the product can be best formulated as $[Cd(H_2L)(CH_3COO)_2]_n{\cdot}2nCH_3COCH_3$ on the basis of microanalysis and TGA. Calcd for $C_{44}H_{56}CdN_4O_{10}$ (%): C, 57.86; H, 6.18; N, 6.13; Cd, 12.31. Found (%): C, 59.03; H, 5.82; N, 5.91; Cd, 12.15. IR (cm^{-1}, KBr): 3450 (s), 1603 (s), 1260 (s), 501 (m), 421 (m).

3. Results and discussion

3.1. IR spectra

As shown in Fig. 1, there are various absorption peaks in the range of 4000–400 cm^{-1} for the ligand H_2L and its Co(II) MOF and Cd(II) CP. In the ligand H_2L, there is a large absorption peak at about 3450 cm^{-1}, which is caused by the stretching vibration of hydroxyl group in the ligand H_2L molecule, the strong absorption peak at about 1603 cm^{-1} belongs to the typical C=N stretching vibration, and the absorption peak at about 1260 cm^{-1} is the typical Ar-O stretching vibration.

Infrared spectrum of H_2L exhibits a strong band at 3450 cm^{-1} which is connected with the phenolic O–H stretching vibration band. However, this band is disappeared in the Co(II) MOF, indicating that the phenolic O–H groups of the ligand are fully deprotonated [49]. A large O–H stretching vibration band in the Co(II) MOF is observed at around 3400 cm^{-1} corresponding to water molecules in the manufactured of KBr lamination. The typical C=N and Ar-O stretching vibrations appear at about 1591 and 1225 cm^{-1}, with significant low wavenumber displacements, indicating the coordination has occurred [58]. In addition, there are two medium absorption peaks at about 513 and 468 cm^{-1}, which are

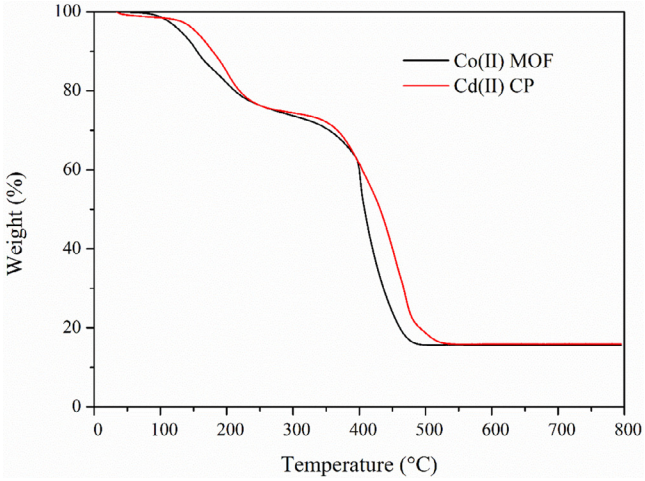

Fig. 18. TGA curves of the Co(II) MOF and Cd(II) CP.

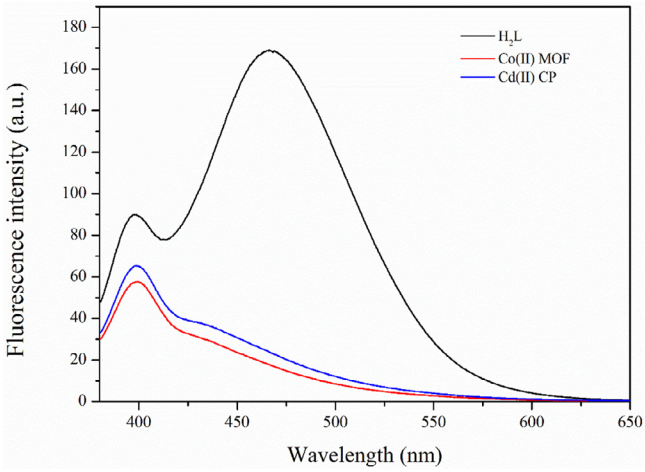

Fig. 19. Fluorescence spectra of H_2L and its Co(II) MOF and Cd(II) CP.

the absorption peaks of Co-O and Co-N bonds [59], showing Co(II) ions are coordinated with the deprotonated ligand $(L)^{2-}$ unit.

Compared with the free ligand H_2L, the absorption peak at about 3450, 1603 and 1260 cm^{-1} in the Cd(II) CP did not change significantly, but there are two new absorption peaks at about 509 and 421 cm^{-1}, which is assigned to the coordination of the Cd(II) ion with acetate O atoms and pyridine N atoms from the unprotonated ligand H_2L [59]. The result is consistent with the single crystal structure.

3.2. UV–Vis spectra analysis

The UV–Vis spectra of H_2L (DMF, 5×10^{-5} M) and its Co(II) MOF and Cd(II) CP (DMF, 5×10^{-5} M) are shown in Fig. 2. In the absorption curve of the free ligand H_2L, there are two strong absorption peaks at *ca.* 271 and 326 nm, which can be attributed to the π-π^* transitions of benzene rings and oxime groups, respectively [60]. Compared with the free ligand H_2L, the absorption peaks of the Co(II) MOF and Cd(II) CP at *ca.* 271 nm decreased significantly, while the absorption peaks at *ca.* 326 nm have red-shift to *ca.* 336 and 338 nm respectively, which may be due to the ligand to metal charge transition (LMCT) [61], these results are consistent with the previous report, and similar to the ligand to metal charge transition in salen-like metal complexes [48].

The titration curves of the Co(II) MOF and Cd(II) CP are shown in Fig. 3. In Fig. 3a, with the addition of Co^{2+} (1×10^{-3} M), the absorption peak intensity at 326 nm increases gradually and shows an obvious red-shift. When 1 equiv. Co^{2+} is add, the absorption peak redshifts to 336 nm and the intensity reaches the maximum, an isoabsorption point appears at *ca.* 291 nm. After continuously added Co^{2+}, the absorption intensity at 336 nm does not change any more. The results of titration show that the optimal ratio of H_2L to Co^{2+} is 1:1. In Fig. 3b, with the addition of Cd^{2+} (1×10^{-3} M), a similar phenomenon appears, and the absorption peak redshifts to 338 nm, and an isoabsorption point appears at *ca.* 302 nm. When 1 equiv. Cd^{2+} is add, the absorption strength at 338 nm will not increase any more, indicating that the optimal combination ratio of H_2L and $Cd^{2+}$is 1:1, which is consistent with the obtained single crystal structure by X-ray diffraction analysis.

Table 1
The crystal data and structure optimization of the Co(II) MOF and Cd(II) CP.

Complex	The Co(II) MOF	The Cd(II) CP
Empirical formula	$C_{71}H_{78}Co_2N_8O_9$	$C_{38}H_{44}CdN_4O_8$
Formula weight	1305.27	797.17
T (K)	100.00(10)	100.00(10)
Wavelength (Å)	MoKα (λ = 0.71073)	CuKα (λ = 1.54184)
Crystal system	tetragonal	triclinic
Space group	$P4_3$	P-1
a (Å)	21.2198(10)	10.5161(8)
b (Å)	21.2198(10)	13.1563(10)
c (Å)	20.8795(14)	18.7244(14)
α (°)	90	99.572(6)
β (°)	90	92.335(6)
γ (°)	90	91.923(6)
V (Å^3)	9401.6(9)	2550.2(3)
Z	4	2
D_{calc} (g·cm^{-3})	0.922	1.038
Absorption coefficient (mm^{-1})	0.397	3.770
F (000)	2744.0	824.0
Crystal size (mm)	0.13 × 0.11 × 0.10	0.12 × 0.1 × 0.09
2θ Range (°)	3.838–49.996	4.792–149.952
Index ranges	$-25 \le h \le 16$ $-23 \le k \le 25$ $-19 \le l \le 24$	$-11 \le h \le 13$ $-16 \le k \le 16$ $-23 \le l \le 22$
Reflections collected	24698	18076
Independent reflections	13968[R_{int}=0.0700, R_{sigma} =0.1401]	9931 [R_{int}=0.0660, R_{sigma}= 0.0865]
data/restraints/parameters	13968/43/825	9931/0/468
GOF	0.971	1.054
Final R_1, wR_2 indices	0.0671, 0.1322	0.0977, 0.2647
R_1, wR_2 indices (all data)	0.1009, 0.1506	0.1195, 0.2892
Largest diff. peak and hole (e.Å^{-3})	0.59/−0.39	3.27/−1.69

3.3. Crystal structure descriptions

The main bond lengths (Å) and angles (°) of the Co(II) MOF and Cd(II) CP are presented in Table 1. The detailed information of hydrogen bonds in the Co(II) MOF and Cd(II) CP are listed in Table 2. The crystal data and structure optimization of the Co(II) MOF and Cd(II) CP are listed in Table 3.

3.3.1. Crystal structure of the Co(II) MOF

The obtained red bulk single crystal was subjected to X-ray diffraction analysis. The Co(II) MOF crystallizes in the tetragonal system, and the space group was $P\ 4_3$. There is no doubt about the obtained Co(II) MOF is the first reported case in the salamo-like complexes [34–36].

There are two Co(II) ions with similar coordination environments in the Co(II) MOF. As shown in Fig. 4, the Co1 ion is located in the N_2O_2 cavity of the completely deprotonated ligand $(L)^{2-}$ unit (the N_2O_2 cavity is composed of the N1, N2, O1 and O4

Table 2
Selected bond lengths (Å) and angles (°) of the Co(II) MOF and Cd(II) CP.

The Co(II) MOF					
Bond	Lengths	Bond	Lengths	Bond	Lengths
Co1-O4	1.976(5)	Co1-N7$^{\#2}$	2.177(6)	Co2-N4	2.146(6)
Co1-O1	2.039(6)	Co1-N1	2.101(7)	Co2-N5	2.114(6)
Co1-N2	2.145(6)	Co2-O5	2.027(5)	Co2-N8$^{\#3}$	2.160(6)
Co1-N3$^{\#1}$	2.207(8)	Co2-O8	2.023(5)	Co2-N6	2.095(6)
Bond	Angles	Bond	Angles	Bond	Angles
O4-Co1-O1	91.1(2)	N2-Co1-N7$^{\#2}$	91.1(2)	O8-Co2-N4	87.2(2)
O4-Co1-N2	85.9(2)	N1-Co1-N2	97.2(3)	O8-Co2-N5	172.2(2)
O4-Co1-N3$^{\#1}$	86.7(3)	N1-Co1-N3$^{\#1}$	95.8(3)	O8-Co2-N8$^{\#3}$	91.2(2)
O4-Co1-N1	176.0(3)	N1-Co1-N7$^{\#2}$	85.6(3)	O8-Co2-N6	85.7(2)
O4-Co1-N7$^{\#2}$	91.9(2)	N7$^{\#2}$-Co1-N3$^{\#1}$	178.4(3)	N4-Co2-N8$^{\#3}$	177.3(2)
O1-Co1-N2	176.8(2)	O5-Co2-N4	94.0(2)	N5-Co2-N4	85.5(2)
O1-Co1-N3$^{\#1}$	89.2(3)	O5-Co2-N5	87.1(2)	N5-Co2-N8$^{\#3}$	96.0(2)
O1-Co1-N1	85.8(2)	O5-Co2-N8$^{\#3}$	83.8(2)	N6-Co2-N4	92.9(2)
O1-Co1-N7$^{\#2}$	90.1(2)	O5-Co2-N6	172.1(2)	N6-Co2-N5	97.3(2)
N2-Co1-N3$^{\#1}$	89.6(3)	O8-Co2-O5	90.8(2)	N6-Co2-N8$^{\#3}$	89.2(2)
$^{\#1}$ 1-Y, −1+X, −1/4+Z $^{\#2}$ 1-X, 1-Y, 1/2+Z $^{\#3}$ -Y, +X, −1/4+Z.					
The Cd(II) CP					
Bond	Lengths	Bond	Lengths	Bond	Lengths
Cd1-O1	2.338(6)	Cd1-O3	2.420(6)	Cd1-N4$^{\#2}$	2.391(6)
Cd1-O1$^{\#1}$	2.613(5)	Cd1-O4	2.271(5)		
Cd1-O2	2.433(6)	Cd1-N1	2.301(5)		
Bond	Angles	Bond	Angles	Bond	Angles
O1-Cd1-O2	53.65(19)	O4-Cd1-O1	112.73(19)	N1-Cd1-O2	124.3(2)
O1-Cd1-O1$^{\#1}$	69.15(18)	O4-Cd1-O1$^{\#1}$	81.00(18)	N1-Cd1-O1	88.67(19)
O1-Cd1-O3	151.76(18)	O4-Cd1-O2	92.4(2)	N1-Cd1-O3	91.26(18)
O1-Cd1-N4$^{\#2}$	123.7(2)	O4-Cd1-O3	55.39(17)	N1-Cd1-N4$^{\#2}$	87.34(19)
O2-Cd1-O1$^{\#1}$	114.14(18)	O4-Cd1-N1	142.86(19)	N4$^{\#2}$-Cd1-O1$^{\#1}$	161.24(18)
O3-Cd1-O1$^{\#1}$	83.12(17)	O4-Cd1-N4$^{\#2}$	103.2(2)	N4$^{\#2}$-Cd1-O2	84.2(2)
O3-Cd1-O2	141.9(2)	N1-Cd1-O1$^{\#1}$	78.95(17)	N4$^{\#2}$-Cd1-O3	84.44(19)
$^{\#1}$ -X, 1-Y, 2-Z $^{\#2}$ −1+X, +Y, 1+Z.					

atoms), and the four atoms form a plane with the Co1 ion, We named this part "Co1-L" (The coordination environment of the Co2 ion is similar to the Co1 ion, and the Co2 ion is located in the N_2O_2 cavity of the deprotonated ligand $(L)^{2-}$ unit, the N_2O_2 cavity is composed by the N5, N6, O5 and O8 atoms, the four atoms form a plane with the Co2 ion, which named it "Co2-L").

The terminal pyridine N3 atom of the "Co1-L" part participates in the coordination of axial position of the N_2O_2 plane (N1, N2, O1 and O4) from another "Co1-L" part, and the terminal pyridine N7 atom of the "Co2-L" part also participates in coordination of another axial position of the N_2O_2 plane (N1, N2, O1 and O4). Similarly, the terminal pyridine N8 atom of the "Co2-L" part participates in the coordination of axial position of the N_2O_2 plane (N5, N6, O5 and O8) from the another "Co2-L" part, and the terminal pyridine N4 atom of the "Co1-L" part also participates in coordination of another axial position of the N_2O_2 plane (N5, N6, O5 and O8). Both Co1 and Co2 ions are six-coordinated octahedral geometric configurations. The "Co1-L" and "Co2-L" moieties are connected through the terminal pyridine N atoms to form the smallest symmetric unit shown in Fig. 5. Since the pyridine and the benzene rings are connected by a single bond, when the complex is formed, the pyridine and the benzene rings will rotated and present different angles (Fig. S4).

The Co1 and Co2 ions were used as the connection points in the smallest symmetric units, and the smallest symmetric unit serves as the connector to form a metal-organic frame with a three-dimensional structure with regular pores in the c-direction (Fig. 6). However, when observing in the *a*-direction, it is found that there is a double helix structure in the structure as shown in Fig. 7. Red and yellow represent two different spiral structures. The two spiral structures intersect each other (Fig. 7), and the interpenetrated spiral structures are connected by the terminal pyridine N atoms of the "Co1-L" and "Co2-L" parts, and finally produce metal organic framework with different sizes of pores (Fig. 8).

In addition, there are 13 pairs of obvious intramolecular hydrogen bonds (C(5)–H(5B)···N(3), C(20)–H(20A)···O(4), C(21)–H(21C)···O(4), C(27)–H(27A)···O(1), C(28)–H(28C)···O(1), C(32)–H(32)···N(6), C(37)–H(37B)···N(8), C(48)–H(48)···O(1), C(51)–H(51C)···O(8), C(60)–H(60A)···O(5), C(61)–H(61C)···O(5), C(64)–H(64)···O(8) and C(67)–H(67)···O(5)) in the Co(II) MOF (Fig. 9a), and two pairs of intermolecular hydrogen bonds (C(46)–H(46)···O(7), C(66)–H(66)···O(9)) between the Co(II) MOF molecules and between the Co(II) MOF and the solvent acetone molecule (Fig. 9b).

3.3.2. Crystal structure of the Cd(II) CP

The obtained colorless bulk single crystal was subjected to X-ray diffraction analysis. The Cd(II) CP crystallizes in the triclinic system, and the space group is P-1. What's interesting is that unlike the previously reported transition metal complexes [62–65], the Cd(II) ion (Cd1) is not located at the N_2O_2 cavity of the ligand H_2L. To our knowledge, this phenomenon is never occurred in the previously reported salen- and salamo-like complexes [45,46,48].

It is well known that Cd(II) is located in the fifth period of the periodic table of elements and has a large ionic radius. When Cd(II) ions coordinate with H_2L, the larger radius of Cd(II) ions cannot enter the N_2O_2 cavity. While Cd(II) generally has a higher coordination number [68], the loss of stable coordination

Table 3
The information about hydrogen bond in the Co(II) MOF and Cd(II) CP, and C–H···π and π···π stacking information in Cd(II) CP.

The Co(II) MOF				
D–H···A	d(D–H)	d(H–A)	d(D–A)	∠D–X–A
C(5)–H(5B)···N(3)	0.9700	2.5500	3.459(13)	156.00
C(20)–H(20A)···O(4)	0.9600	2.4400	3.018(12)	118.00
C(21)–H(21C)···O(4)	0.9600	2.3900	3.031(11)	123.00
C(27)–H(27A)···O(1)	0.9600	2.4100	2.984(14)	118.00
C(28)–H(28C)···O(1)	0.9600	2.4900	3.101(13)	122.00
C(32)–H(32)···N(6)	0.9300	2.5900	3.161(11)	120.00
C(37)–H(37B)···N(8)	0.9700	2.5700	3.480(11)	157.00
C(51)–H(51C)···O(8)	0.9600	2.3600	2.988(11)	123.00
C(60)–H(60A)···O(5)	0.9600	2.4200	3.030(9)	121.00
C(61)–H(61C)···O(5)	0.9600	2.4300	3.034(9)	121.00
C(64)–H(64)···O(8)	0.9300	2.5300	3.013(9)	113.00
C(67)–H(67)···O(5)	0.9300	2.5600	3.139(10)	120.00
C(46)–H(46)···O(7)	0.9300	2.4700	3.093(8)	124.00
C(48)–H(48)···O(1)	0.9300	2.4700	3.041(11)	120.00
C(66)–H(66)···O(9)	0.9300	2.5600	3.454(11)	162.00
C-H···π	H-Cg	X–Cg		∠C–H–Cg
C(6)–H(6)···Cg(8)	2.81	3.726(9)		170
C(64)–H(64)···Cg(4)	2.35	2.966(9)		124
C(65)–H(65)···Cg(3)	2.56	3.061(8)		114
C(71)–H(71B)···Cg(10)	2.96	3.887(12)		161
The Cd(II) CP				
D–H···A	d(D–H)	d(H–A)	d(D–A)	∠D–X–A
O(5)–H(5)···N(2)	0.8200	1.8600	2.593(8)	148.00
O(8)–H(8)···N(3)	0.8200	1.9200	2.647(10)	147.00
C(2)–H(2A)···O(3)	0.9800	2.5800	3.490(10)	155.00
C(5)–H(5A)···O(1)	0.9500	2.4600	3.151(8)	129.00
C(5)–H(5A)···O(4)	0.9500	2.4600	3.220(9)	136.00
C(19)–H(19A)···O(5)	0.9800	2.3200	2.956(11)	122.00
C(21)–H(21A)···N(3)	0.9900	2.5900	2.926(10)	100.00
C(32)–H(32)···O(2)	0.9500	2.5500	3.174(10)	123.00
C(33)–H(33)···O(3)	0.9500	2.5500	3.212(10)	127.00
C(36)–H(36A)···O(8)	0.9800	2.4200	3.041(13)	121.00
C(38)–H(38C)···O(8)	0.9800	2.2900	2.969(11)	126.00
C(18)–H(18C)···O(5)	0.9800	2.3400	3.004(10)	125.00
C–H···π	H-Cg	X–Cg		∠C–H–Cg
C(21)–H(21B)···Cg(1)	2.83	3.769(8)		158
C(22)–H(22B)···Cg(2)	2.94	3.919(10)		171
Cg(3)···Cg(3) 3.908(4)				

site of the N_2O_2 cavity leads to the failure to meet the higher coordination number. However, there are some acetate anions in the solution, which can coordinate with Cd(II) ions. As shown in Fig. 10, two bidentate chelated acetate anions (O1, O2, O3 and O4 atoms) are coordinated to Cd1 ion, and two Cd1 ions with the same coordination environment are bridged by O1 atom of one of the acetate anions to form $Cd_2(OAc)_2$ unit. Using the $Cd_2(OAc)_2$ unit as the junction point and H_2L as the linker, the $Cd_2(OAc)_2$ unit was coordinated with terminal pyridine N atoms (N1 and N4) of H_2L to form a coordination polymer with specification holes. Among them, Cd1 ion is a seven-coordinated single cap triangular prism geometry (Fig. 11). As shown in Fig. 12, the coordination polymer has a large cavity with a pore size of 25.26 × 17.49 Å^2.

In the Cd(II) CP, there are 12 pairs of obvious intramolecular hydrogen bonds (O(5)–H(5)···N(2), O(8)–H(8)···N(3), C(2)–H(2A)···O(3), C(5)–H(5A)···O(1), C(5)–H(5A)···O(4), C(18)–H(18C)···O(5), C(19)–H(19A)···O(5), C(21)–H(21A)···N(3), C(32)–H(32)···O(2), C(33)–H(33)···O(3), C(36)–H(36A)···O(8) and C(38)–H(38C)···O(8)) are observed (Fig. 13). In addition, there are two kinds of C–H···π interaction (C(21)–H(21B)···Cg(1) and C(22)–H(22B)···Cg(2)) of the Cd(II) CP (Fig. 14a), and have one kind of π···π stacking interaction (Cg(3)···Cg(3)) in the Cd(II) CP (Fig. 14b). Through C–H···π and π···π stacking interactions to form a 2-D supramolecular structure, as shown in Fig. 15.

Both the Co(II) MOF and Cd(II) CP were obtained from the same ligand H_2L, but the two complexes possess different structures. On the one hand, the radius of the Co(II) and Cd(II) ions are quite different. The Cd(II) ion cannot enter the N_2O_2 cavity to participate in the coordination, but coordinate with the free acetate in the solution and form the $Cd_2(OAc)_2$ connecting unit. On the contrary, the N_2O_2 cavity can provide stable four coordination sites, which is easier to stabilize the Co(II) ions. On the other hand, the common coordination number of the Co(II) ion is five or six, while the Cd(II) ion needs higher coordination number [68]. The terminal pyridine N atoms of H_2L is easy to participate in the coordination with the Co(II) and Cd(II) ions. In conclusion, the Co(II) ion can located at the N_2O_2 cavity of the ligand $(L)^{2-}$ unit, its terminal pyridine N atoms occupied the two axial positions, while the Cd(II) ion only coordinated with the terminal pyridine N atoms of H_2L. Finally, the pyridine ring in the Co(II) MOF is cis, while in the Cd(II) CP is trans.

3.4. Hirshfeld surface analyses

Hirshfeld surface analysis [66] is carried out by selecting the smallest symmetrical unit of the Co(II) MOF and Cd(II) CP. Figs. 16 and 17 represent the Hirshfeld surfaces of the Co(II) MOF and Cd(II) CP, and are mapped to d_{norm}, shape index and curvature, respectively. In the map of d_{norm}, the red region represents the O···H/H···O interactions (C–H···O hydrogen bonding contact on the surface) in the Co(II) MOF and Cd(II) CP, the darker the color, the stronger the interaction. The white spots on the surface are due to the H···H interactions, while the blue areas in the surface illustrates that there is no interaction because the atoms are far away from each other. Comparing the d_{norm} of the Co(II) MOF and Cd(II) CP, it is found that the interaction of O···H/H···O in the Cd(II) CP is significantly stronger than that of the Co(II) MOF. This is consistent with the crystal structures observed. Shape index and curvature can be used to identify stacking interactions in the Co(II) MOF and Cd(II) CP. For the Co(II) MOF, red or blue triangle (bow tie pattern) was observed in the shape index (black circle), and there are flat surface patches in the curvature (red circle), which indicates that there are C–H···π stacking interactions. While in the Cd(II) CP, more red or blue triangles (bow tie pattern) and flat surface patches were observed in shape index (black circle) and curvature (red circle), which indicated the existence of C–H···π stacking and π···π interaction. In the two-dimensional fingerprint, gray represents the whole fingerprint, while the blue area represents the proportion of each short-range effect. In the Co(II) MOF, taking the O···H/H···O interactions as an example, the O···H interaction is mainly concentrated in the peak position at the bottom right of the fingerprint, while the H···O interaction is mainly concentrated in the peak position at the top left of the fingerprint. The proportion of O···H/H···O interactions is 7.0%. The proportions of C···H/H···C, N···H/H···N and H···H interactions are 15.7%, 3.2% and 67.5%, respectively. Therefore, H···H interaction is the main interaction in the Co(II) MOF. In the Cd(II) CP, the proportions of the O···H/H···O, C···H/H···C, N···H/H···N and H···H interactions are 17.0%, 12.6%, 2.2% and 60.3%, respectively. Therefore, H···H interaction is the main interaction in the Cd(II) CP.

3.5. TGA analyses

Weigh out 5 mg of the Co(II) MOF and Cd(II) CP respectively, control the heating rate at 10 °C/min, the thermal stability of the Co(II) MOF and Cd(II) CP are analyzed using thermogravimetric analysis. As shown in Fig. 18, the weight loss of the Co(II) MOF

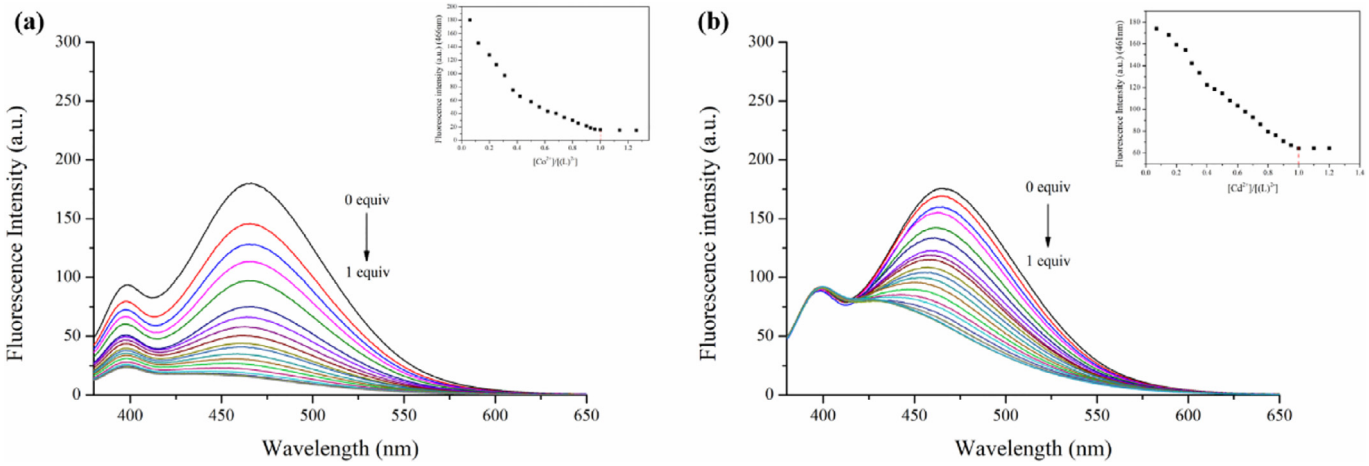

Fig. 20. (a) Continuous addition of Co^{2+} (1×10^{-3} M) to H_2L (5×10^{-5} M) leads to a change in fluorescence intensity; (b) Continuous addition of Cd^{2+} (1×10^{-3} M) to H_2L (5×10^{-5} M) leads to a change in fluorescence intensity.

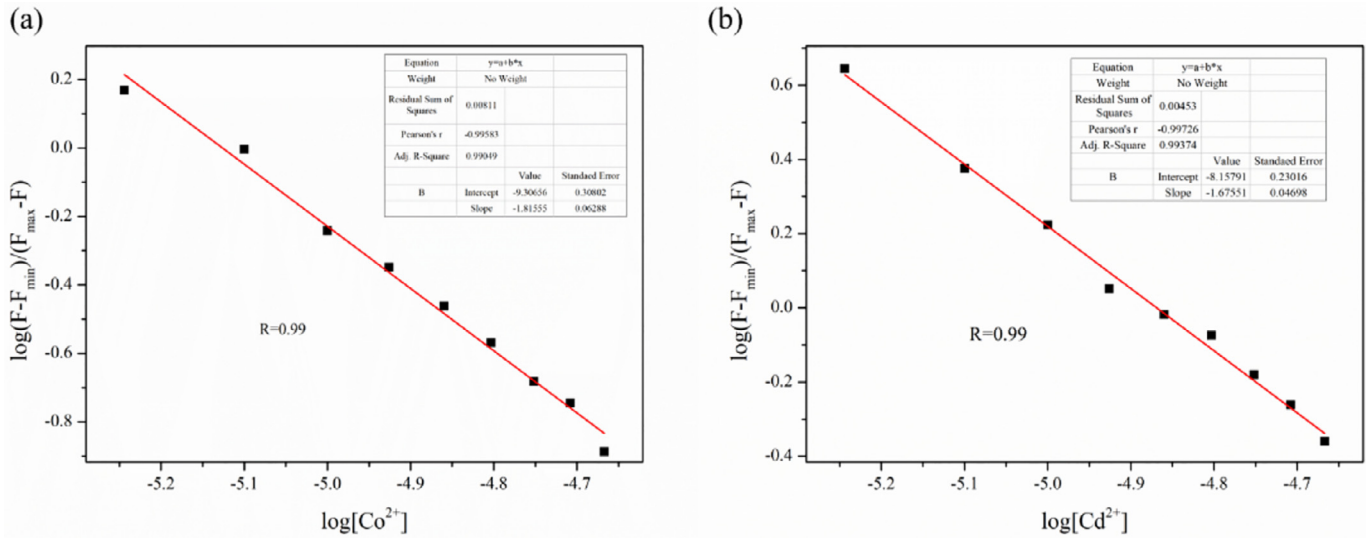

Fig. 21. (a) The linear fitting of the binding constants of H_2L and Co^{2+} ion; (b) The linear fitting of the binding constants of H_2L and Cd^{2+} ion.

is mainly divided into two stages. The weight loss is 22.5% in the range of 85–230 °C, and the solvent molecules in the Co(II) MOF are calculated as 13.1%, so this should be weight loss due to the loss of three acetone and one pyridine molecules in the Co(II) MOF. In the range of 372–502 °C, the weight loss is caused by the decomposition of the main framework of the Co(II) MOF. After 600 °C, the weight will not be lost, the remaining weight is 15.4%, and the theoretical analysis of CoO is 11.2%. The two values are close, so it is inferred that the Co(II) MOF will generate its oxide after being heated at 600 °C. The weight loss of the Cd(II) CP can be divided into two stages. The weight loss is 23.8% in the range of 46–240 °C, and the solvent molecules in the Cd(II) CP are calculated as 19.7%, so this should be weight loss due to the loss of two acetone molecules in the Cd(II) CP. While in the range of 360–532 °C, it belongs to the decomposition of the main framework of the Cd(II) CP. After 600 °C, the weight will not be lost, the remaining weight is 16.1%, and the theoretical analysis of CdO is 12.9%. The two values are close, so it can be concluded that Cd(II) CP will generate its oxide after being heated at 600 °C. Thermogravimetric analyses show that the Co(II) MOF and Cd(II) CP could withstand the high temperature of more than 350 °C and keep the structure intact, indicating that both Co(II) MOF and Cd(II) CP have good thermal stabilities.

3.6. Fluorescence properties

With 350 nm as excitation wavelength and 10 / 20 nm as slit, the ligand H_2L and its Co(II) MOF and Cd(II) CP used anhydrous ethanol as solvent. The fluorescence spectra of H_2L (5×10^{-5} M) and its Cd(II) CP and Co(II) MOF (5×10^{-5} M) are given in Fig. 19. The ligand H_2L has an emission peak at approximately 466 nm, which may be due to the π-π^* transition within the ligand [67]. While the emission peaks of the Co(II) MOF and Cd(II) CP at 466 nm disappeared significantly, decreased fluorescence intensity of the Co(II) MOF and Cd(II) CP may be due to the introduction of the Co(II) and Cd(II) ions into the ligand [68]. A small absorption peak appears at approximately 452 and 440 nm, respectively, there are significant blue-shifts, which may be due to the occurrence of ligand-to-metal charge transition (LMCT) [61].

The titration curves of the Co(II) MOF and Cd(II) CP are shown in Fig. 20. In Fig. 20a, with the addition of Co^{2+} (1×10^{-3} M), the fluorescence intensity at 466 nm decreases gradually, and shown a slight blue-shift. When 1 equivalent Cd^{2+} is add, the emission peak at 466 nm is moved to 452 nm, which is due to the coordination between Co^{2+} and the ligand, resulting in the ligand to metal charge transition (LMCT) [69]. After continuing to add Co^{2+}, the fluorescence intensity at 452 nm will not change any more.

The titration results show that the optimal binding ratio of the ligand H_2L to Co^{2+} is 1:1, which is consistent with the single crystal structure obtained by X-ray diffraction analysis. In Fig. 20b, a similar phenomenon occurs with the addition of Cd^{2+} (1×10^{-3} M), and the emission peak is moved to 440 nm. When 1 equivalent Co^{2+} is add, the fluorescence intensity at 440 nm does not decrease any more, indicating that the optimal binding ratio of the ligand H_2L to Cd^{2+} is 1:1, which is consistent with the obtained single crystal structure. The results of the titration are brought into the Hill equation [70] to calculate the binding constant. The binding constants of the ligand H_2L with Co^{2+} and Cd^{2+} ions are calculated to be 3.05×10^5 M^{-1} and 2.03×10^5 M^{-1}, respectively (Fig. 21).

4. Conclusions

A novel salamo-like ligand H_2L containing double terminal pyridine groups was synthesized and characterized. Two structurally different Co(II) MOF and Cd(II) CP, $[\{Co(L)\}_2]_n \cdot nCH_3COCH_3$ and $[Cd(H_2L)(CH_3COO)_2]_n$ were obtained by self-assembly of H_2L with Cd(II) and Co(II) ions. In which, a first reported salamo-like metal-organic framework (MOF) with regular pore sizes is self-assembled via H_2L and Co(II) ion, while a never found and structurally novel coordination polymer (CPs) is self-assembled from the Cd(II) ion and the unprotonated ligand H_2L adopting N_2O_2 cavity not involved in the coordination. TGA analyses show that the Co(II) MOF and Cd(II) CP have good thermal stabilities. Fluorescence titrations indicate the binding constants of the ligand H_2L with Co^{2+} and Cd^{2+} ions are calculated to be 3.05×10^5 M^{-1} and 2.03×10^5 M^{-1}, respectively. Theoretical analyses of the presences of various interactions in the Co(II) MOF and Cd(II) CP are carried out by Hirshfeld surfaces analyses.

Author statement

No conflict of interest exits in the submission of this manuscript, and manuscript is approved by all authors for publication. I would like to declare on behalf of my coauthors that the work described was original research that has not been published previously, and not under consideration for publication elsewhere, in whole or in part. All the authors listed have approved the manuscript that is enclosed. In addition, we solemnly declare that the article is original and unpublished and is not being considered for publication elsewhere.

Declaration of Competing Interest

The authors declare no competing financial interests.

CRediT authorship contribution statement

Ji-Fa Wang: Supervision. **Tao Feng:** Supervision. **Ya-Juan Li:** Supervision. **Yin-Xia Sun:** Supervision. **Wen-Kui Dong:** Supervision. **Yu-Jie Ding:** Supervision.

Acknowledgments

This work was supported by the National Natural Science Foundation of China (21761018), Science and Technology Program of Gansu Province (18YF1GA057) and the Program for Excellent Team of Scientific Research in Lanzhou Jiaotong University (201706), three of which are gratefully acknowledged. Computations were done using National Supercomputing Center in Shenzhen, P. R. China.

Supplementary materials

Supplementary material associated with this article can be found, in the online version, at doi:10.1016/j.molstruc.2021.129950.

Appendix A. Supplementary data

Crystallographic data have been deposited with the Cambridge Crystallographic Data centre as supplementary publication, No. CCDC – 2014475 and 2014474 for the Co(II) MOF and Cd(II) CP. Copies of these data can be obtained free of charge on application to CCDC, 12 Union Road, Cambridge CB21EZ, UK (Telephone: +(44)−01223–762910; Fax: +44–1223–336033; E-mail: deposit@ccdc.cam.ac.uk). These data can be also obtained free of charge at www.ccdc.cam.ac.uk/conts/retrieving.html.

References

[1] X. Han, Q.C. Xia, J.J. Huang, Y. Liu, C.X. Tan, Y. Cui, Chiral covalent organic frameworks with high chemical stability for heterogeneous asymmetric catalysis, J. Am. Chem. Soc. 139 (2017) 8693–8697.
[2] A.M. Shultz, A.A. Sarjeant, O.K. Farha, J.T. Hupp, S.T. Nguyen, Post-synthesis modification of a metal-organic framework to form metallosalen-containing MOF materials, J. Am. Chem. Soc. 133 (2011) 13252–13255.
[3] O G.A. E.xford, R.Q. Snurr, L.J. Broadbelt, Hybrid quantum mechanics/molecular mechanics investigation of (salen)Mn for use in metal-organic frameworks, Ind. Eng. Chem. Res. 49 (2010) 10965–10973.
[4] Y.B. Huang, T.F. Liu, J.X. Lin, J. Lu, Z.J. Lin, R. Cao, Homochiral nickel coordination polymers based on salen(Ni) metalloligands: synthesis, structure, and catalytic alkene epoxidation, Inorg. Chem. 50 (2011) 2191–2198.
[5] F.J. Song, C. Wang, J.M. Falkowski, L.Q. Ma, W.B. Lin, Isoreticular chiral metal-organic frameworks for asymmetric alkene epoxidation: tuning catalytic activity by controlling framework catenation and varying open channel sizes, J. Am. Chem. Soc. 132 (2010) 15390–15398.
[6] T.U. Yoon, M.J. Kim, A.R. Kima, J.H. Kang, D. Jia, Y.S. Bae, Cu-impregnated metal–organic frameworks for separation and recovery of CO from blast furnace gas, J. Ind. Eng. Chem. 87 (2020) 102–109.
[7] S.B. Xia, Y.X. Yan, W.J. Huang, R.M. Yang, H.B. Suo, J.M. Liu, F.X. Cheng, J.J. Liu, In-situ synthesis of nanocomposite from metal-organic frameworks template for high-performance rechargeable batteries, J. Power Sources 464 (2020) 228247.
[8] E.H. Ryu, J.H. Lee, Y.S. Lee, J.M. Gu, S. Huh, S.J. Lee, Size-controlled cubic coordination polymer nanoparticles from chiral dipyridyl Zn-salen, Inorg. Chem. Commun. 14 (2011) 1648–1651.
[9] J.J. Liu, S.B. Xia, D. Liu, J.Y. Hou, H.B. Suo, F.X. Cheng, Multifunctional naphthalene diimide-based coordination polymers: photochromism and solventchromism, Dyes Pigm. 177 (2020) 108269.
[10] J.W. Zhang, C.R. Wang, W.H. Liu, S. Xu, B.Q. Liu, Two kinds of 2,4-dichlorobenzoate-based lanthanide coordination polymers tuned by 4,4′-bipyridine: syntheses, structures, photoluminescence, and magnetism, Inorg. Chim. Acta 508 (2020) 119648.
[11] Y. Kang, Y.H. Zhang, P.P. Sun, P.B. Huang, X.H. Yu, Q. Shi, B. Tian, J. Gao, F.N. Shi, Bimetallic coordination polymer composites: a new choice of electrode materials for lithium ion batteries, Solid State Ionics 350 (2020) 115310.
[12] Y.F. Jing, D.J. Young, Q. Huang, Y. Mi, S.C. Zhang, F.L. Hu, Amino group decorated coordination polymers for enhanced detection of folic acidm, Spectrochim. Acta, Part A 238 (2020) 118443.
[13] H. Xu, R.H. Sabina, R.H. Javier, P.C. Javier, J. Jordi, I. Inhar, M. Daniel, A first cyclodextrin-transition metal coordination polymer, Cryst. Growth Des. 16 (2016) 5598–5602.
[14] F. Juvenal, D. Fortin, P.D. Harvey, A platinum(II) organometallic building block for the design of emissive Copper(I) and Silver(I) coordination Polymers, Inorg. Chem. 59 (2020) 7117–7134.
[15] X.G. Guo, S. Qiu, X.T. Chen, Y. Gong, X.Q. Sun, Postsynthesis modification of a metallosalen-containing metal−organic framework for selective Th(IV)/Ln(III) separation, Inorg. Chem. 56 (2017) 12357–12361.
[16] J.Q. Dong, C.X. Tan, K. Zhang, Y. Liu, J. Paul, J.W. Jiang, Y. Cui, Chiral NH-controlled supramolecular metallacycles, J. Am. Chem. Soc. 139 (2017) 1554–1564.
[17] J.W. Li, Y.M. Fan, Y.W. Ren, J.H. Liao, C.R. Qi, H.F. Jiang, Development of isostructural porphyrin-salen chiral metal-organic frameworks though postsynthetic metalation based on single-crystal to single-crystal transformation, Inorg. Chem. 57 (2018) 1203–1212.
[18] Q.C. Xia, C. Yuan, Y.X. Li, Y. Cui, Design and assembly of a chiral composite metal–organic framework for efficient asymmertric sequential transformation of alkenes to amino alcohols, Chem. Comm. 55 (2019) 9136–9139.
[19] L.L. Wang, J.M. Wang, C.B. Fan, C.B. Bi, X.D. Zhang, M. Zhang, M. Wang, Y.H. Fan, Two novel Co (II)-coordination polymers as bifunctional materials for efficient photocatalytic degradation of dyes and electrocatalytic water oxidation, Appl. Organomet. Chem. (2020) e5767.

[20] J.J. Liu, Y.W. Lu, J. Li, W.B. Lu, UV and X-ray dual photochromic properties of three CPs based on a new viologen ligand, Dyes Pigm. 177 (2020) 108266.
[21] T. Nakamura, S. Tsukuda, T. Nabeshima, Double-circularly connected saloph–belt macrocycles generated from a bis-armed bifunctional monomer, J. Am. Chem. Soc. 141 (2019) 6462–6467.
[22] Y. Sakata, S. Chiba, M. Miyashita, T. Nabeshima, S. Akine, Ligand exchange strategy for tuning of helicity inversion speeds of dynamic helical tri(saloph) metallocryptands, Chem. Eur. J. 25 (2019) 2962–2966.
[23] A. Sumiyoshi, Y. Chiba, R. Matsuoka, T. Noda, T. Nabeshima, Efficient luminescent properties and cation recognition ability of heavy group 13 element complexes of N2O2- and N2O4-type dipyrrins, Dalton Trans. 48 (2019) 13169–13175.
[24] C.H. Ryu, S.W.H. Kwak, H.W. Lee, J.H. Lee, H. Hwang, M. Kim, Y. Chung, Y. Kim, M. Park, M.H. Lee, Carbazole-appended salen−indium conjugate systems: synthesis and enhanced luminescence efficiency, Inorg. Chem. 58 (2019) 12358–12364.
[25] S. Akine, S. Piao, M. Miyashita, T. Nabeshima, Monomeric and dimeric red/NIR-fluorescent dipyrrin–germanium complexes: facile monomer–dimer interconversion driven by acid/base additions, Tetrahedron Lett. 54 (2013) 6541–6544.
[26] T. Nabeshima, M. Yamamura, Cooperative formation and functions of multimetal supramolecular systems, Pure Appl. Chem. 85 (2013) 763–776.
[27] S. Akine, Z. Varadi, T. Nabeshima, Synthesis of planar metal complexes and the stacking abilities of naphthalenediol-based acyclic and macrocyclic salen-type ligands, Eur. J. Inorg. Chem. 35 (2013) 5987–5998.
[28] Y.Q. Pan, Y. Zhang, M. Yu, Y. Zhang, L. Wang, Newly synthesized homomultinuclear Co (II) and Cu (II) bissalamo-like complexes: structural characterizations, Hirshfeld analyses, fluorescence and antibacterial properties, Appl. Organomet. Chem. 34 (2020) e5441.
[29] Y.F. Cui, Y. Zhang, K.F. Xie, W.K. Dong, A newly synthesized heterobimetallic Ni^{II}-Gd^{III} salamo-BDC-based coordination polymer: structural characterization, DFT calculation, fluorescent and antibacterial properties, Crystals 9 (2019) 596.
[30] L.W. Zhang, Y. Zhang, Y.F. Cui, M. Yu, W.K. Dong, Heterobimetallic [NiIILnIII] (Ln = Sm and Tb) N2O4-donor coordination polymers: syntheses, crystal structures and fluorescence properties, Inorg. Chim. Acta 506 (2020) 119534.
[31] X.X. An, C. Liu, Z.Z. Chen, K.F. Xie, W.K. Dong, An unexpected trinuclear cobalt(II) complex based on a half-salamo-like ligand: synthesis, crystal structure, Hirshfeld surface analysis, antimicrobial and fluorescent properties, Crystals 9 (2019) 602.
[32] S.Z. Zhang, J. Chang, H.J. Zhang, Y.X. Sun, Y. Wu, Y.B. Wang, Synthesis, crystal structure and spectral properties of binuclear Ni(II) and cubane-like Cu4(μ3-O)4 cored tetranuclear Cu(II) complexes based on coumarin schiff base, Chin. J. Inorg. Chem. 36 (2020) 503–514.
[33] L. Wang, Z.L. Wei, M. Yu, Y.Q. Pan, Y. Zhang, W.K. Dong, Multihalogen-substituted salamo-type Mn(II) complexes: syntheses, crystal structures, Hirshfeld analyses and fluorescence properties, Chin. J. Inorg. Chem. 35 (2019) 1791.
[34] Q.P. Kang, X.Y. Li, Z.L. Wei, Y. Zhang, W.K. Dong, Symmetric containing-PMBP N_2O_2-donors nickel(II) complexes: syntheses, structures, Hirshfeld analyses and fluorescent properties, Polyhedron 165 (2019) 38–50.
[35] L.Z. Liu, M. Yu, X.Y. Li, Q.P. Kang, W.K. Dong, Syntheses, structures, Hirshfeld analyses and fluorescent properties of two Ni(II) and Zn(II) complexes constructed from a bis(salamo)-like ligand, Chin. J. Inorg. Chem. 35 (2019) 1283–1294.
[36] Y. Zhang, L.Z. Liu, Y.D. Peng, N. Li, W.K. Dong, Structurally characterized trinuclear nickel(II) and copper(II) salamotype complexes: syntheses, Hirshfeld analyses and fluorescent properties, Transit. Met. Chem. 44 (2019) 627–639.
[37] Y.Q. Pan, X. Xu, Y. Zhang, Y. Zhang, W.K. Dong, A highly sensitive and selective bis(salamo)-type fluorescent chemosensor for identification of Cu^{2+} and the continuous recognition of S^{2-}, arginine and lysine, Spectrochim. Acta A 229 (2020) 117927.
[38] Z.L. Wei, L. Wang, J.F. Wang, W.T. Guo, Y. Zhang, W.K. Dong, Two highly sensitive and efficient salamo-like copper(II) complex probes for recognition of CN^-, Spectrochim. Acta A 228 (2020) 117775.
[39] L. Wang, Z.L. Wei, Z.Z. Chen, C. Liu, W.K. Dong, Y.J. Ding, A chemical probe capable for fluorescent and colorimetric detection to Cu^{2+} and CN^- based on coordination and nucleophilic addition mechanism, Microchem. J. 155 (2020) 104801.
[40] C. Liu, Z.L. Wei, H.R. Mu, W.K. Dong, Y.J. Ding, A novel unsymmetric bis(salamo)-based chemosensor for detecting Cu^{2+} and continuous recognition of amino acids, J. Photochem. Photobio. A 397 (2020) 112569.
[41] L. Wang, Z.L. Wei, C. Liu, W.K. Dong, J.X. Ru, Synthesis and characterization for a highly selective bis(salamo)-based chemical sensor and imaging in living cell, Spectrochim, Acta A 239 (2020) 118496.
[42] H.R. Mu, M. Yu, L. Wang, Y. Zhang, Y.J. Ding, Catching S^{2-} and Cu^{2+} by a highly sensitive and efficient salamo-like fluorescence-ultraviolet dual channel chemosensor, Phosphorus Sulfur Silicon Relat. Elem. 195 (2020) 730–739.
[43] L.Z. Liu, L. Wang, M. Yu, Q. Zhao, Y. Zhang, Y.X. Sun, W.K. Dong, A highly sensitive and selective fluorescent "off-on-off" relay chemosensor based on a new bis(salamo)-type tetraoxime for detecting Zn^{2+} and CN^-, Spectrochim. Acta A 222 (2019) 117209.
[44] H.R. Mu, X.X. An, C. Liu, Y. Zhang, W.K. Dong, Structurally characterized self-assembled heterobimetallic Ni(II)—Eu(III)-salamo-bipyridine coordination polymer: synthesis, photophysical and antimicrobial properties, J. Struct. Chem. 61-7 (2020) 1218–1229.
[45] C. Liu, X.X. An, Y.F. Cui, K.F. Xie, W.K. Dong, Novel structurally characterized hetero-bimetallic [$Zn(II)_2M(II)$] (M = Ca and Sr) bis(salamo)-type complexes: DFT calculation, Hirshfeld analyses, antimicrobial and fluorescent properties, Appl. Organomet. Chem. 34 (2020) e5272.
[46] Y. Zhang, M. Yu, Y.Q. Pan, Y. Zhang, L. Xu, X.Y. Dong, Three rare heteromultinuclear 3d-4f salamo-like complexes constructed from auxiliary ligand 4,4′-bipy: syntheses, structural characterizations, fluorescence and antimicrobial properties, Appl. Organomet. Chem. 34 (2020) e5442.
[47] L. Wang, Y.Q. Pan, J.F. Wang, Y. Zhang, Y.J. Ding, A highly selective and sensitive half-salamo-based fluorescent chemosensor for sequential detection of Pb(II) ion and Cys, J. Photochem. Photobio. A 400 (2020) 112719.
[48] X.Y. Li, Q.P. Kang, C. Liu, Y. Zhang, W.K. Dong, Structurally characterized homo-trinuclear Zn^{II} and hetero-pentanuclear [$Zn^{II}_4Ln^{III}$] complexes constructed from an octadentate bis(Salamo)-based ligand: Hirshfeld surfaces, fluorescence and catalytic properties, New J. Chem. 43 (2019) 4605–4619.
[49] Q. Zhao, X.X. An, L.Z. Liu, W.K. Dong, Syntheses, luminescences and Hirshfeld surfaces analyses of structurally characterized homo-trinuclear Zn^{II} and hetero-pentanuclear Zn^{II}-Ln^{III} (Ln=Eu, Nd) bis(salamo)-like complexes, Inorg. Chim. Acta 490 (2019) 6–15.
[50] Q.P. Kang, X.Y. Li, L. Wang, Y. Zhang, W.K. Dong, Containing-PMBP N_2O_2-donors transition metal(II) complexes: synthesis, crystal structure, Hirshfeld surface analyses and fluorescence properties, Appl. Organomet. Chem. 33 (2019) e5013.
[51] X.Y. Dong, Q.P. Kang, X.Y. Li, J.C. Ma, W.K. Dong, Structurally characterized solvent-Induced homotrinuclear cobalt(II) N_2O_2-donor bisoxime-type complexes, Crystals 8 (2018) 139.
[52] J. Chang, S.Z. Zhang, Y. Wu, H.J. Zhang, Y.X. Sun, Three supramolecular trinuclear nickel(II) complexes based on salamo–type chelating ligand: syntheses, crystal structures, solvent effect, Hirshfeld surface analysis and DFT calculation, Transit. Met. Chem. 45 (2020) 279–293.
[53] M. Yu, Y. Zhang, Y.Q. Pan, L. Wang, Two novel copper(II) salamo-based complexes: syntheses, X-ray crystal structures, spectroscopic properties and Hirshfeld surfaces analyses, Inorg. Chim. Acta 509 (2020) 119701.
[54] X.X. An, Q. Zhao, H.R. Mu, W.K. Dong, A new half-salamo-based homo-trinuclear nickel(II) complex: crystal structure, Hirshfeld surface analysis, and fluorescence properties, Crystals 9 (2019) 101.
[55] Y.X. Sun, Y.Q. Pan, X. Xu, Y. Zhang, Unprecedented dinuclear CuII N,O-donor complex: synthesis, structural characterization, fluorescence property, and Hirshfeld analysis, Crystals 9 (2019) 607.
[56] W.I. Madison, SAINT-Plus, Bruker Analytical X-ray System Bruker, Billerica, MA, USA, 1999.
[67] G.M. Sheldrick, SADABS, Program for Empirical Absorption Correction of Area Detector Data, University of Gottingen: Gottingen, Germany, 1996.
[58] X.X. An, Z.Z. Chen, H.R. Mu, L. Zhao, Investigating into crystal structures and supramolecular architectures of four newly synthesized hetero-octanuclear [Cu^{II}_4-Ln^{III}_4] (Ln = Sm, Eu, Tb and Dy) complexes produced by a hexadentate bisoxime chelate ligand, Inorg. Chim. Acta 511 (2020) 119823.
[59] A. Majumder, G.M. Rosair, A. Mallick, N. Chattopadhyay, S. Mitra, Synthesis, structures and fluorescence of nickel, zinc and cadmium complexes with the N,N,O-tridentate Schiff base N-2-pyridylmethylidene-2-hydroxy-phenylamine, Polyhedron 25 (2006) 1753.
[60] S. Akine, Y. Morita, F. Utsuno, T. Nabeshima, Multiple folding structures mediated by metal coordination of acyclic multidentate ligand, Inorg. Chem. 48 (2009) 10670–10678.
[61] R.N. Bian, J.F. Wang, Y.J. Li, Y. Zhang, W.K. Dong, Fluorescent chemical sensor based on double N_2O_2 cavities for continuous recognition of Cu^{2+} and Al^{3+}, J. Photochem. Photobiol. A. 400 (2020) 112829.
[62] X. Xu, R.N. Bian, S.Z. Guo, W.K. Dong, Y.J. Ding, A new asymmetric salamo-based chemical sensor for dual channel detection of Cu^{2+} and $B_4O_7^{2-}$, Inorg. Chim. Acta 513 (2020) 119945.
[63] Y.D. Peng, Y. Zhang, Y.L. Jiang, Z.L. Ren, F. Wang, L. Wang, An unsymmetric salamo-like chemosensor for fuorescent recognition of Zn^{2+}, J. Fluores. 30 (2020) 1049–1061.
[64] Y. Zhang, Y.J. Li, S.Z. Guo, T. Fu, L. Zhao, A series of heterobimetallic Ni(II)–Ln(III) (Ln = La, Ce, Pr and Nd) coordination polymers derived from 3–EtOsalamo and dicarboxylates: syntheses, crystal structures and fluorescence properties, Transit. Met. Chem. 45 (2020) 485–492.
[65] Y. Zhang, Y.Q. Pan, M. Yu, X. Xu, W.K. Dong, Single-armed salamo-like dioxime and its multinuclear Cu(II), Zn(II) and Cd(II) complexes: syntheses, structural characterizations, Hirshfeld analyses and fluorescence properties, Appl. Organomet. Chem. 33 (2019) e5240.
[66] L. Rohl, A. Moret, M. Kaminsky, W. Claborn, K. McKinnon, J.J. Kahr, Hirshfeld surfaces identify inadequacies in computations of intermolecular interactions in crystals: pentamorphic 1,8-dihydroxyanthraquinone, Cryst. Growth Des. 8 (2015) 4517–4525.
[67] L. Xu, M. Yu, L.H. Li, J.C. Ma, W.K. Dong, A heterotetranuclear zinc(II)—Cerium(IV) salamo complex possessing deca- and dodeca-coordinated cerium(IV) atoms: synthesis, structure, and photophysical properties, J. Struct. Chem. 60 (2019) 1358.
[68] C.Y. Guo, Y.Y. Wang, K.Z. Xu, H.L. Zhu, P. Liu, Q.Z. Shi, S.M. Peng, Crystal structures, bioactivities and fluorescent properties of four diverse complexes with a new symmetric benzimidazolic ligand, Polyhedron 27 (2008) 3529–3536.
[69] M. Yu, H.R. Mu, L.Z. Liu, N. Li, Y. Bai, X.Y. Dong, Syntheses, structures and Hirshfeld analyses of trinuclear Ni(II) salamo-type complexes, Chin. J. Inorg. Chem. 35 (2019) 1109.
[70] Z.L. Wei, L. Wang, S.Z. Guo, Y. Zhang, W.K. Dong, A high-efficiency salamo-based copper(II) complex double-channel fluorescent probe, RSC Adv. 9 (2019) 41298.